

THE PENNSYLVANIA STATE UNIVERSITY
SCHREYER HONORS COLLEGE

DEPARTMENT OF ENGINEERING SCIENCE AND MECHANICS

INVESTIGATING PERFORMANCE LIMITING DEFECTS IN SILICON CARBIDE
BIPOLAR JUNCTION TRANSISTORS USING ELECTRICALLY DETECTED MAGNETIC
RESONANCE

ROBERT S. CARRIER
SPRING 2019

A thesis
submitted in partial fulfillment
of the requirements
for a baccalaureate degree
in Engineering Science
with honors in Engineering Science

Reviewed and approved* by the following:

Patrick M. Lenahan
Distinguished Professor of Engineering Science and Mechanics
Thesis Supervisor and Honors Advisor

Saptarshi Das
Assistant Professor of Engineering Science and Mechanics
Faculty Reader

Judith A. Todd
Department Head
P.B. Breneman Chair and Professor of Engineering Science and Mechanics

*Signatures are on file in the Schreyer Honors College and the Engineering Science and Mechanics office.

ABSTRACT

SiC is a wide bandgap semiconductor whose properties make it promising for use in high voltage, high temperature, high frequency, and high radiation environments where silicon devices often fail. SiC BJTs are used in military, space exploration, and aerospace applications. However, much work is needed to improve the current gain in SiC BJTs, which is limited by recombination centers throughout the defects. SDR is an EDMR technique that can identify recombination centers that directly affect device performance. Very little data is available in literature pertaining to SDR in SiC BJTs and p-n junctions. In this paper, low field SDR and near zero field magnetic resonance (NZFMR) are performed on the base-collector junction of a 4H-SiC bipolar junction transistor (BJT) in order to identify nuclear hyperfine (NHF) patterns that reveal information about performance-limiting recombination centers in the depletion regions of the BJT. The main goal of this research was to compare the NHF patterns in the low-field SDR and NZFMR measurements to each other and to hyperfine patterns in literature in order to identify performance limiting recombination centers present in the device and demonstrate the spectroscopic capabilities of low-field SDR and NZFMR, which require much less power and machinery than high-field EDMR or conventional electron paramagnetic resonance (EPR).

However, no NHF patterns were undeniably identified in the four NZFMR signals or the three low-field SDR signals. The magnetometer sensitivity of the four NZFMR signals were analyzed and compared to another 4H-SiC BJT, which revealed that the SDR signals in this paper were weak. This fact partly explains why no NHF patterns could be distinguished from the noise in the signals even after long periods of signal averaging. The low-field SDR and NZFMR signals were compared which revealed an intriguing fact that the low-field and zero-field

responses were of opposite polarity. The low-field SDR mechanism caused a positive change in recombination current, while the zero-field SDR mechanisms caused a negative change in recombination current. The defects responsible for the SDR responses were not identified because the NZFMR response was not yet useful without hyperfine patterns and the g values of the low-field response were not yet comparable with g values in literature. Ultimately, the spectroscopic ability of SDR on 4H-SiC BJTs was not well demonstrated.

TABLE OF CONTENTS

LIST OF FIGURES	iii
LIST OF TABLES	iv
ACKNOWLEDGEMENTS	v
Chapter 1 Introduction	1
1.1 Problem Statement	1
Chapter 2 Background Information and Literature Review.....	3
2.1 Physics of Semiconductors.....	3
2.2 Physics of a p-n junction	7
2.3 Overview of the Bipolar Junction Transistor	10
2.4 Review of Current Status of SiC BJTs.....	14
2.4.1 Background Information of Device of Interest.....	16
2.5 Magnetic Resonance Spectroscopy	17
2.5.1 Explanation of Electron Paramagnetic Resonance	18
2.5.2 Electrically Detected Magnetic Resonance (EDMR)	21
2.5.3 Near Zero-Field Magnetoresistance	23
2.6 Review of Past Research on EDMR in SiC BJTs	25
2.6.1 SiC p-n Junctions as Deep Space Magnetometers.....	29
Chapter 3 Experimental Methods	31
3.1 EDMR Spectrometers	31
3.2 Procedure	33
Chapter 4 Results and Discussion.....	37
4.1 SPA Measurements	37
4.2 Validation of SDR Response.....	39
4.3 NZFMR on Base-Collector Junction Results	41
4.4 Magnetometer Sensitivity of the Base-Collector Junction	48
4.5 Low-Field SDR Measurements with Oscillating RF Field	50
4.6 Base-emitter Junction and Common Emitter Biasing	54
Chapter 5 Conclusion and Future Work	55
Appendix MATLAB Code For Plotting Theoretical Recombination Current.....	57
BIBLIOGRAPHY	58

LIST OF FIGURES

Figure 1: Generation of electron-hole pairs in a semiconductor	4
Figure 2: Dopant atoms in the Si crystal lattice [1].....	5
Figure 3: Fermi-Dirac Distribution at different temperatures [1]	6
Figure 4: Diagram of how the Fermi-level and carrier concentration change with doping [1]7	
Figure 5: Energy band diagram of a p-n junction in equilibrium [3]	8
Figure 6: Effect of biasing on current in a p-n junction [1]	9
Figure 7: Current v. Voltage in a p-n junction diode [3].....	10
Figure 8: Band diagram of an n-p-n BJT [4].....	10
Figure 9: Band diagram of a p-n-p structure BJT [4].....	11
Figure 10: Band diagram of a p-n-p BJT in common-emitter operating mode [2]	11
Figure 11: (a) common-emitter schematic (b) amplification of base current [2]	13
Figure 12: Common-emitter characteristic curves of a BJT [5].....	13
Figure 13: (a) Simplified diagram of BJT and (b) top face of actual BJT [8].....	16
Figure 14: I-V characteristics of device used in experiments [8].....	17
Figure 15: Zeeman splitting of electron spin state energy [13].....	18
Figure 16: NHF interactions causes splitting in the resonance signal [13]	20
Figure 17: Spin Dependent Recombination in a p-n junction [10]	22
Figure 18: a) Theoretical recombination current and b) SDR amplitude [11]	27
Figure 19: Schematic of Low-Field EDMR Spectrometer [5]	31
Figure 20: I-V Curves for BJT junctions	37
Figure 21: Common-emitter characteristic curves	38
Figure 22: NZFMR signal amplitude versus forward bias voltage	40
Figure 23: Theoretical relationship between recombination current and forward bias in the 4H-SiC pn junction.....	40

Figure 25: Second Derivative of NZFMR Signal 1	42
Figure 24: First NZFMR signal, averaged over 3572 scans	42
Figure 26: NZFMR Signal 2 using spectrometer 2	45
Figure 27: Second derivative of NZFMR signal 2.....	45
Figure 28: NZFMR signal 3 using spectrometer 3.....	46
Figure 29: Derivative of NZFMR signal 3.....	46
Figure 30: NZFMR Signal 4 using first spectrometer.....	47
Figure 31: Derivative of NZFMR Signal 4.....	47
Figure 32: Derivative of SDR wide scan	51
Figure 33: 200G wide SDR measurement with 151MHz RF oscillating field.....	51
Figure 34: Low-Field SDR response with RF oscillating field of 151Hz.....	52

LIST OF TABLES

Table 1: Properties of SiC and other semiconductors [6]	15
Table 2: NZFMR signal amplitude at different forward bias voltages.....	40
Table 3: Magnetometer sensitivity of the four NZFMR signals	48

ACKNOWLEDGEMENTS

I would first like to thank Dr. Lenahan for advising me throughout the entire thesis process, as well as being a great instructor and mentor. His class ESC 312 sparked my interest in the field of semiconductor devices, and I am excited to be involved in this field in the future. I would also like to thank every graduate student in the lab. Each of them were very helpful whenever I had questions or needed help. I would especially like to thank Colin McKay and Jim Ashton, who helped me often throughout this project. Finally, I would like to acknowledge the other undergraduates in the lab. Everyone supported and motivated each other to get their projects done.

Chapter 1

Introduction

1.1 Problem Statement

SiC is a wide bandgap semiconductor whose properties make it promising for use in high voltage, high temperature, high frequency, and high radiation environments where silicon devices often fail. SiC BJTs are used in military, space exploration, and aerospace applications. However, much work is needed to improve the current gain, which is limited by recombination centers throughout the defects. These recombination centers limit the amount of charge carriers that can flow through a BJT, which decreases their performance. One specific application of a SiC p-n junction is in a solid-state magnetometer which uses the near-zero field magnetic resonance (NZFMR) in order to detect very small changes in magnetic fields in outer space. Spin dependent recombination (SDR) is a technique of electrically detected magnetic resonance (EDMR) that allows for the detection of electrically active recombination centers at deep levels within a semiconductor band gap. Typically SDR is performed with high frequency oscillating magnetic fields and at very large magnetic fields which requires expensive and complex instrumentation as well as a lot of energy. However, SDR can also be performed at low magnetic fields with a lower frequency oscillating magnetic field or even without an oscillating magnetic field which only requires magnetic fields near zero. These measurements require much cheaper spectrometers that can basically be built from scratch using many different electrical instruments.

However, there is much less research in the areas of low-field and zero-field EDMR, especially in 4H-SiC devices.

In this paper, low field SDR and near zero field magnetic resonance (NZFMR) are performed on the base-collector junction of a 4H-SiC bipolar junction transistor (BJT) in order to identify NHF (NHF) patterns that reveal information about performance-limiting recombination centers in the depletion regions of the BJT. The main goal of this research was to compare the NHF patterns in the low-field SDR and NZFMR measurements to each other and to hyperfine patterns in literature in order to identify performance limiting recombination centers present in the device and demonstrate the spectroscopic capabilities of low-field SDR and NZFMR.

Chapter 2

Background Information and Literature Review

It is important to understand the physics of a bipolar junction transistor (BJT) before studying one with EDMR. The BJT was the first type of transistor invented in 1947 by Shockley, Bardeen, and Brattain. A BJT is a three terminal device with an emitter, base and collector. It can be used as both an amplifier and a switch. The device is two p-n junctions in close proximity, so before delving into the physics of a BJT, it is important to talk about the basics of semiconductor physics and the p-n junction.

2.1 Physics of Semiconductors

A semiconductor is a material that can act as both a conductor and an insulator depending on the conditions applied to the material. Quantum mechanics dictates that atoms have discrete energy levels that an electron can occupy. When atoms come together to form molecular solids, these discrete energy levels interact to form discrete energy bands. In semiconductors, the two important energy bands are the valence band and the conduction band. An electron in the valence band is held within the bond of two atoms, and therefore it cannot move within the material and conduct a current. However, as shown in Figure 1, if energy is added to the system, the electron

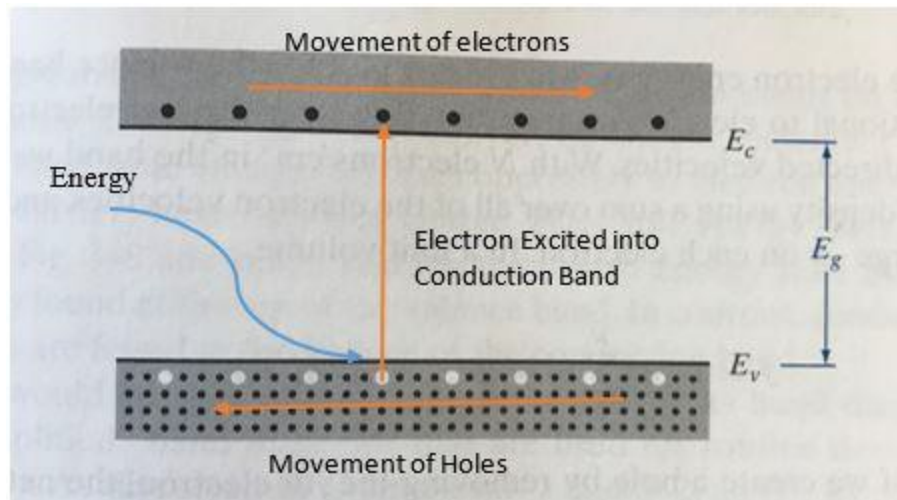


Figure 1: Generation of electron-hole pairs in a semiconductor

can become excited, break free from the bond and transition into the conduction band. In the conduction band, the electron is free to move throughout the material which generates a current. When the electron is excited from the valence band into the conduction band, it leaves behind an empty space or a “hole.” This hole is considered to be a positive charge carrier, because it is the absence of negative charge, and it can move through the valence band as other valence electrons fill in the empty space. Therefore, when an electron is excited into the conduction band, it generates an electron-hole pair (EHP). The difference in energy between the valence band and the conduction band is called the bandgap, and it is on the order of 1eV for most semiconductors. A charge carrier cannot occupy an energy level in between the band gap in the ideal scenario. However, in real materials there are defects which can have energy levels within the bandgap.

A perfect semiconductor crystal that has no added impurity atoms is called an intrinsic semiconductor. An intrinsic semiconductor has no charge carriers at 0K, and the only charge carriers are thermally generated EHPs at higher temperatures [1]. Intrinsic semiconductors are still not very good conductors because the intrinsic number of charge carriers ($n_i = \sim 10^{10} \text{ cm}^{-3}$ in silicon) is a relatively small number for current to be generated. The way to make

semiconductors more conductive is by doping, which is a process where another element is introduced into the semiconductor crystal in order to create a predominance of electrons or holes. For example, arsenic (As) has one more electron than silicon (Si). As shown in Figure 2, if an As atom replaces a Si atom in the lattice, four valence electrons from the As will form bonds with nearby silicon atoms, but there will be one extra electron left that is free to move through the material and generate a current. The same process can be done to create more holes by using an element like Boron (B) which has one less electrons than Si and, therefore, will create a hole where a Si bonding electron used to be. Atoms used for n-type doping are called donor atoms and their concentration is denoted at N_D . Atoms used for p-type doping are called acceptor atoms and their concentration is denoted as N_A .

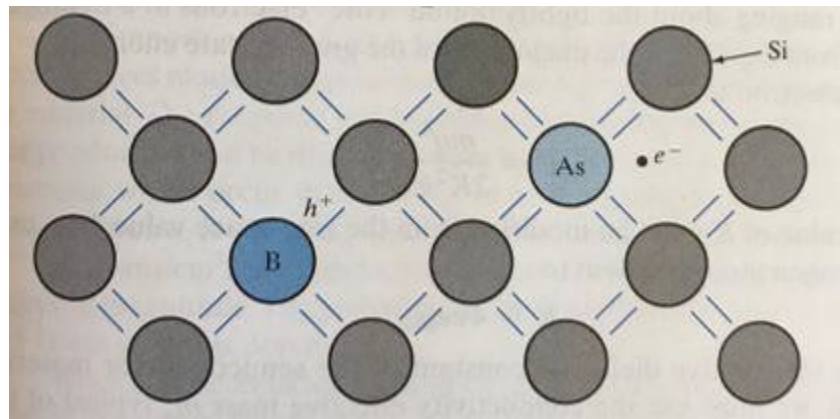


Figure 2: Dopant atoms in the Si crystal lattice [1]

The process of doping changes what is known as the Fermi-energy of the semiconductor which is the energy level at which the probability of finding an electron (or hole) is one-half [1]. This energy level is always within the bandgap, so there is never actually an electron present there (unless there is a defect). The probability of finding an electron at a certain energy is represented by the Fermi-Dirac distribution, shown in Figure 3 and given by

$$f(E) = \frac{1}{1 + e^{(E-E_F)/kT}}$$

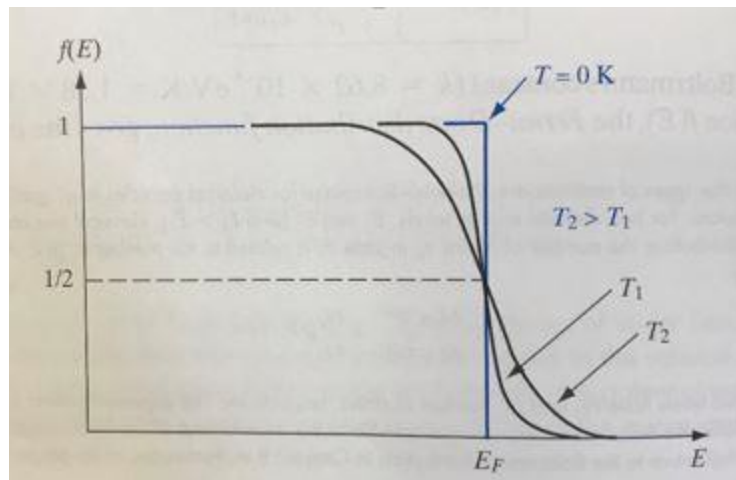


Figure 3: Fermi-Dirac Distribution at different temperatures [1]

where $f(E)$ is the probability of occupation, k is Boltzmann's constant, and T is the temperature. At 0K, the probability of finding an electron goes from 100% to the left of E_F (the valence band) to 0% to the right of E_F (the conduction band). The opposite is true for the probability of finding a hole. The distribution flattens slightly as temperature increases because there is more energy for electrons to be excited into the conduction band, and therefore the probability increases closer to the conduction band.

In an intrinsic semiconductor, the Fermi-level is in the middle of the band gap, so there is a very low probability of finding an electron in the conduction band. However, doping a semiconductor n-type will cause E_F to move closer to the conduction band which increases the probability that an electron is in the conduction band, as shown in Figure 4. The same is true for holes in p-type doping.

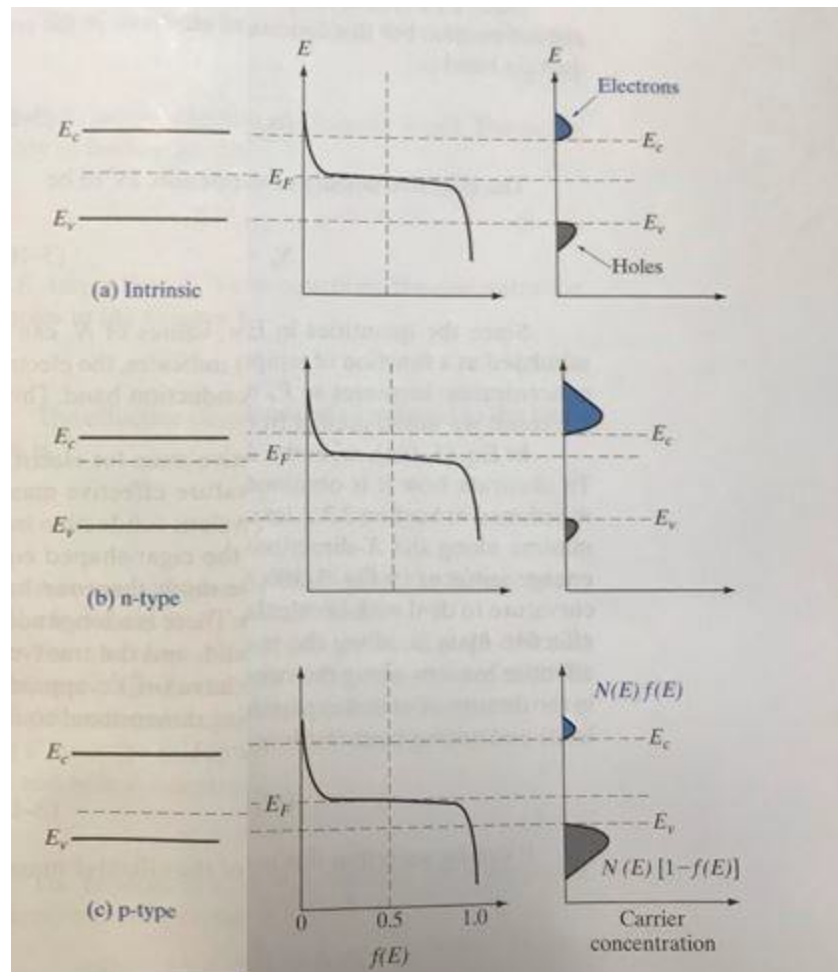


Figure 4: Diagram of how the Fermi-level and carrier concentration change with doping [1]

2.2 Physics of a p-n junction

The p-n junction is a fundamental structure in electronic semiconductor devices. A p-n junction is formed when a p-type and an n-type semiconductor are put together. The basic band diagram is shown in Figure 5. The n-type material has a much higher concentration of electrons in the conduction band, than the p-type, and vice versa for holes in the valence band. When the two materials are put together, there is a diffusion current of electrons (red dots) from n-type to p-type because there is a much higher concentration of electrons in the n-type conduction band

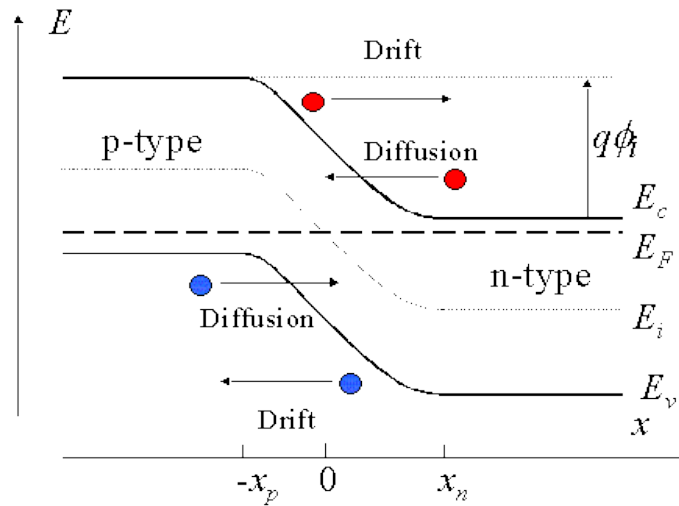


Figure 5: Energy band diagram of a p-n junction in equilibrium [3]

than the p-type conduction band [1]. There is also diffusion of holes (blue dots) from the p-type valence band into the n-type valence band. The electrons leave behind positively charged, uncompensated donor ions (N_d^+), which creates a positive space charge on the n side, and the holes leave behind negatively charged, uncompensated acceptor ions (N_A^-), which create a negative space charge on the p-side [1]. This charge build-up at the junction generates an electric field which causes a drift current of electrons and holes opposing the diffusion current. In equilibrium, these four currents in Figure 5 are equal, so no net current flows. The presence of an electric field means that there is a potential difference between the n-side and p-side called the built-in potential V_0 . This built-in potential acts as a barrier against a net current flow in the p-n junction in equilibrium.

In order to get current to flow in a p-n junction, an external voltage must be applied. When a more positive voltage (V_f) is applied to the p-side, the potential barrier decreases to $V_0 - V_f$ because the electrostatic potential on the p-side becomes less negative, and the energy bands shift down. This condition is called forward bias, and current flows under forward bias because

electrons and holes are able to diffuse across the smaller barrier. The holes and electrons move in opposite directions, which generates a total current in one direction because they have opposite signs. The opposite of forward bias is called reverse bias when a more negative voltage V_r is applied to the p side. Under reverse bias, the potential barrier increases to $V_0 + V_r$ and current does not flow. As shown in Figure 6, the drift current of holes and electrons is constant, and the biasing changes the diffusion current across the barrier [1]. The current vs. voltage graph of a p-n junction diode is shown in Figure 7. Ideally, the current will increase very sharply with an increase in forward bias.

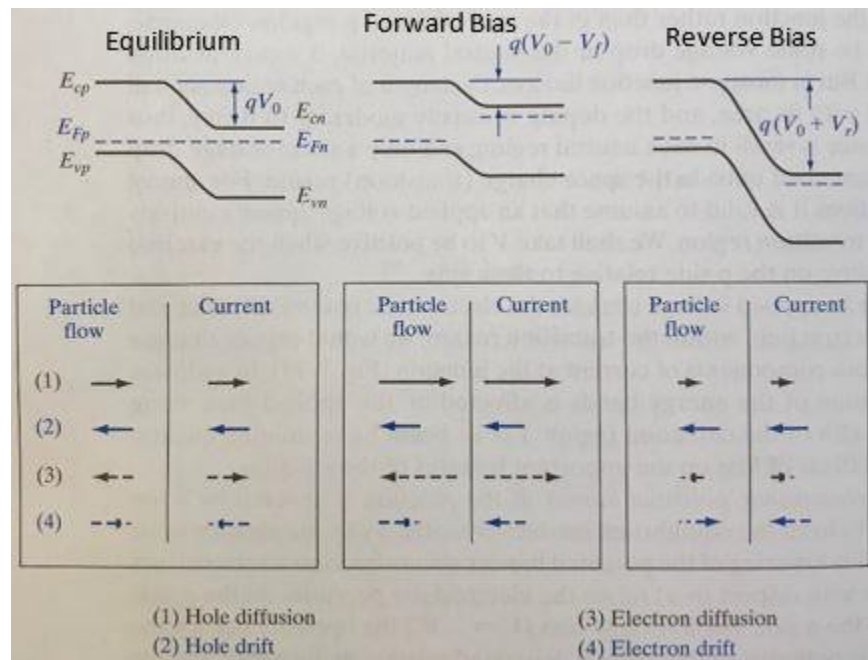


Figure 6: Effect of biasing on current in a p-n junction [1]

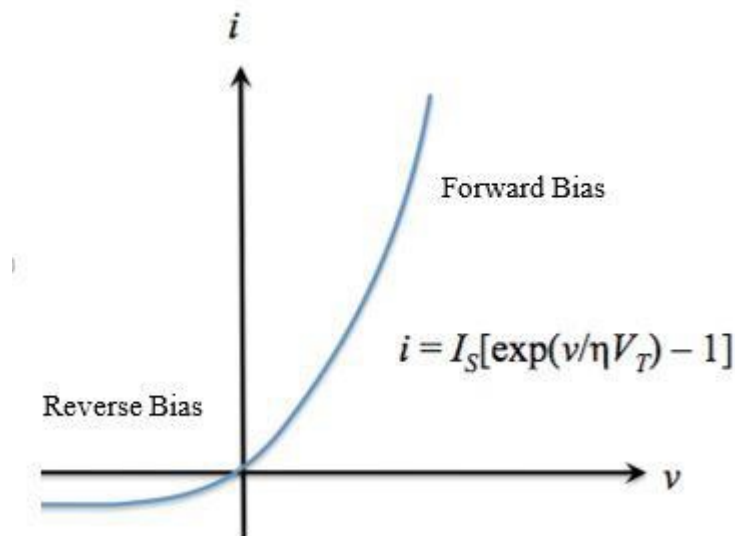


Figure 7: Current v. Voltage in a p-n junction diode [3]

2.3 Overview of the Bipolar Junction Transistor

A bipolar junction transistor is essentially two p-n junctions in close proximity. There can either be a p-n-p BJT, or an n-p-n BJT. The three terminals are the emitter, base, and collector. Figures 8 and 9 show the equilibrium band diagrams of the n-p-n and p-n-p structures, respectively. The emitter is doped more heavily than the collector because the emitter is the

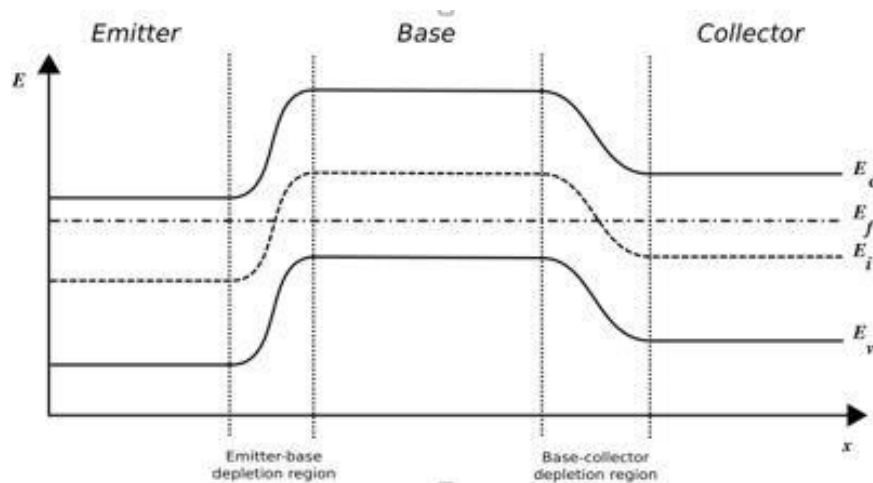


Figure 8: Band diagram of an n-p-n BJT [4]

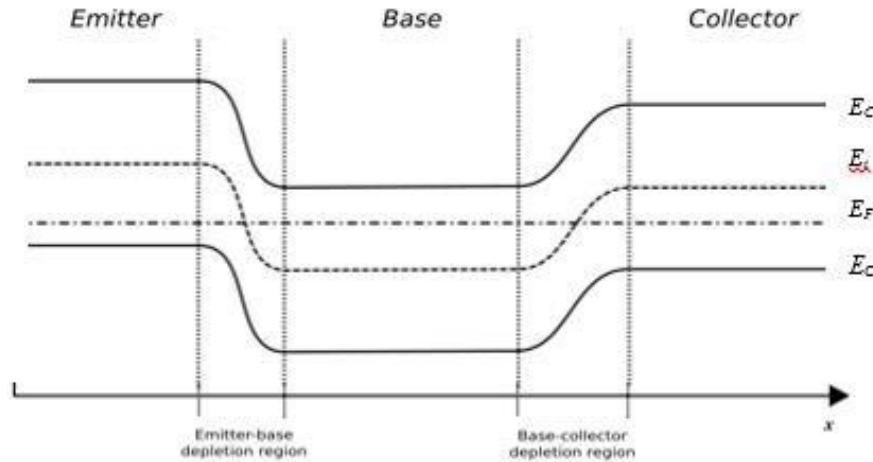


Figure 9: Band diagram of a p-n-p structure BJT [4]

source of charge carriers in the transistor. The example BJT in this section will be a p-n-p structure because most literature explains it in this way. However, the 4H-SiC BJT used in the experiments in this paper is an n-p-n structure. The operation of the two configurations is essentially just a mirror image, where holes are the dominant charge carrier in the p-n-p, and electrons are the dominant charge carrier in the n-p-n.

Under the most common operating conditions of a BJT, the emitter-base junction is forward biased and the base-collector junction is reverse biased. This is illustrated for a p-n-p transistor in Figure 10. The forward bias on the emitter-base junction allows holes to travel into

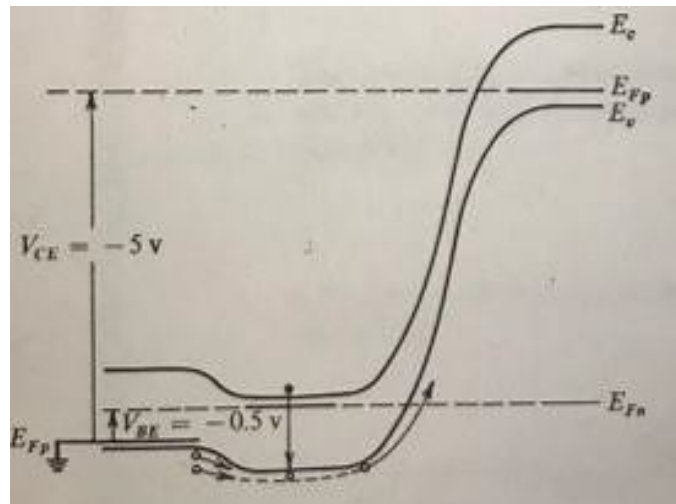


Figure 10: Band diagram of a p-n-p BJT in common-emitter operating mode [2]

the n-type base region, where the holes can diffuse across the base region and are collected by the p-type collector because of the reverse bias. The base must be sufficiently thin so that the holes do not recombine with electrons in the conduction band before they reach the collector.

There are other sources of current in a BJT besides the movement of holes from emitter to collector. Not all holes will reach the collector because there will be some recombination in the base region. Also, because of the forward bias on the emitter-base junction, some electrons will diffuse from the base into the emitter. The emitter must be very heavily doped so that the current is dominated by holes being injected into the base rather than the electrons injected into the emitter [2]. There will also be recombination of holes and electrons in the space charge region of the emitter-base junction [2]. These three sources of electron current mean that electrons will flow into the base, which generate a positive current out of the base [2]. Therefore, the total emitter current I_E is equal to the sum of collector current I_C due to holes being injected and the base current I_B :

$$I_E = I_C + I_B .$$

Two important quantities in the characterization of BJTs are the common-base current gain α and the common-emitter current gain β which are defined as

$$\alpha \equiv \frac{I_C}{I_E} \text{ and } \beta \equiv \frac{I_C}{I_B} .$$

In an ideal transistor, α will be very close to unity, and β will be large. The usefulness of a BJT comes from the fact that β is a large value, meaning a small base current can generate a large collector current. In this sense, a BJT can be used as an amplifier. Figure 12 shows that, in common-emitter configuration, as the base current increases so does the collector current. In this figure, since the collector current is on the order of 1mA, a good transistor should have the base current on the order of 10 uA, which corresponds to a $\beta=100$. Also, Figure 12 shows that V_{CE}

does not impact the amount of current that much in the active region. In Figure 11, an AC current signal with an amplitude of 0.02 mA is applied to the base, and the output is a collector current with an amplitude of 2 [2]. This corresponds to a β of about 100.

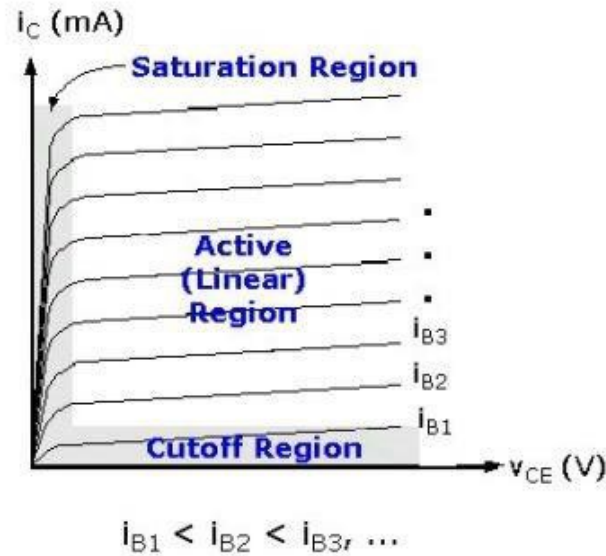


Figure 12: Common-emitter characteristic curves of a BJT [5]

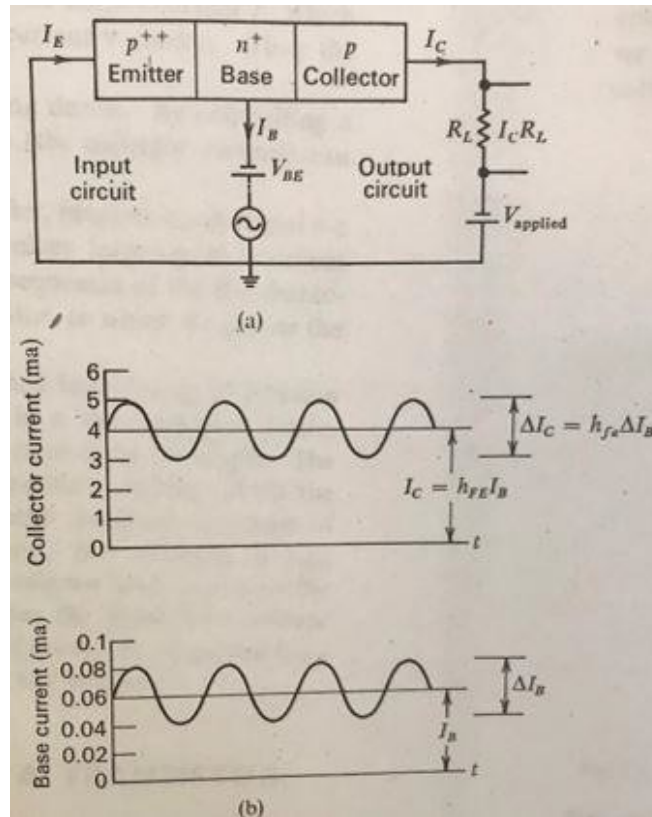


Figure 11: (a) common-emitter schematic (b) amplification of base current [2]

Having a large common-emitter current gain β is the most important characteristic of a BJT. One factor that limits the gain is the presence of recombination centers in the emitter-base junction, the base-collector junction, and throughout the base. These recombination centers limit the amount of charge carriers that can reach the collector, which means more base current is needed to supply the necessary collector current.

2.4 Review of Current Status of SiC BJTs

Silicon-carbide (SiC) offers numerous benefits compared to silicon for use in semiconductor devices at high temperature, high power, high frequency, and in high radiation environments. Silicon devices are not able to operate above 250°C, and operation temperatures between 300°C and 550°C are desired for aerospace applications, nuclear power instruments, satellites, and space exploration [6]. SiC has been shown to operate reliably at these high temperatures [6]. SiC has a much larger band gap than Si, ten times higher critical breakdown voltage, and about 3 times higher thermal conductivity, which means SiC devices can operate at higher temperature, higher voltage, higher frequencies and produce larger currents [6]. SiC is also much more resistant to high radiation environments [6]. In addition to advantages over silicon, SiC has advantages over other wide band gap semiconductors. A thermal oxide can be grown on SiC, which makes device fabrication easier, and the processing of SiC substrates is more matured than other large band gap semiconductors [6]. Table 1 summarizes the properties of SiC against other large band gap semiconductors as well as silicon.

Another reason that SiC is interesting is that it is part of a family of materials that have almost an infinite number of polytypes [6]. Each of the polytypes exhibit different electronic

Table 1: Properties of SiC and other semiconductors [6]

Property	Si	GaAs	GaN	3C-SiC	6H-SiC	4H-SiC
Bandgap E_g (eV at 300k)	1.12	1.43	3.4	2.4	3.0	3.2
Critical electric field E_c (V/cm)	$2.5 \cdot 10^5$	$3 \cdot 10^5$	$3 \cdot 10^6$	$2 \cdot 10^6$	$2.5 \cdot 10^6$	$2.2 \cdot 10^6$
Thermal Conductivity, γ (W/cmK at 300K)	1.5	0.5	1.3	3-4	3-4	3-4
Saturated electron drift velocity v_{sat} (cm/s)	$1 \cdot 10^7$	$1 \cdot 10^7$	$2.5 \cdot 10^7$	$2.5 \cdot 10^7$	$2 \cdot 10^7$	$2 \cdot 10^7$
Electron Mobility μ_n (cm ² /V-s)	1350	8500	1000	1000	500	950
Hole Mobility μ_p (cm ² /V-s)	480	400	30	40	80	120

properties, which makes SiC a versatile material. These polytypes are differentiated by the stacking sequence of the tetrahedral bonded SiC cell [6]. The three basic subcategories for the polytypes are cubic (C), hexagonal (H), and rhombohedral (R). The polytype of SiC that is studied in this paper is 4H-SiC, which has a stacking periodicity of 4 units, and has an equal number of cubic and hexagonal bonds [6]. 4H-SiC has emerged as a more popular material than 6H-SiC because it has a higher electron mobility, as shown in Table 1, and its mobility is also less anisotropic than 6H-SiC [6]. The more isotropic electron mobility means that orientation of the crystal lattice is not as important in 4H-SiC devices.

Many types of SiC solid state devices are currently commercially available. However, there is still more research needed to improve the performance of these devices. Power devices that are commercially available include rectifiers based on Schottky Diodes, and switches based on MOSFETs, JFETs, and BJTs [7]. The main advantages of SiC BJTs over FETs are their low conduction loss as well as more reliable performance at higher junction temperatures [6,7]. Also BJTs are easy to connect in parallel because current gain decreases and on-resistance increases as temperature increases [6,7]. The main drawback of the BJT is that it requires a continuous base

current for control, whereas a MOSFET can be operated as an enhancement mode device, where it is normally-off, so there is less power needed [6,7]. This fact makes it necessary to increase the current gain in SiC BJTs, so that they require less base current to operate at high collector currents. There is still research needed to improve the current gain in SiC BJTs, and one goal of this paper is to identify defects that limit the current gain in a 4H-SiC BJT.

2.4.1 Background Information of Device of Interest

The device investigated in the experiments in this paper was an NPN BJT fabricated by Cree Corporation and supplied by the Army Research Laboratory. The collector was an n-type 4H-SiC substrate, with an n-type drift layer 14 μm thick and doped at 5×10^{15} donors per cm^{-3} [8]. The base was a 0.25 μm thick p-type layer doped at $1 \times 10^{18} \text{ cm}^{-3}$ [8]. The emitter layer was 2 μm thick and heavily doped with nitrogen [8]. Figure 13 shows a simplified structure of the BJT. The emitter and base contacts are on the top, and the collector contact is on the bottom.

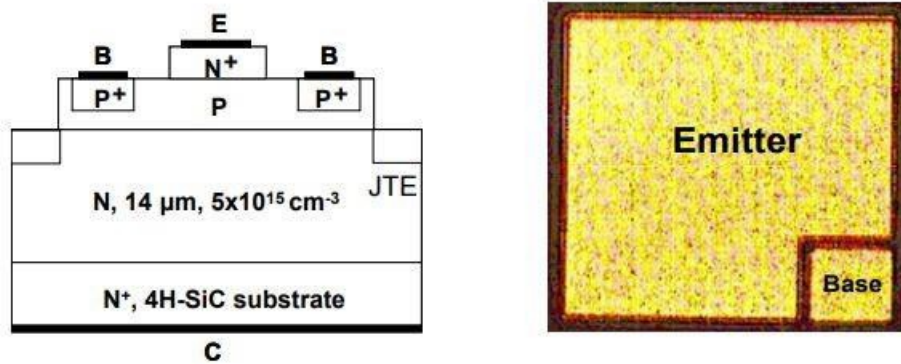


Figure 13: (a) Simplified diagram of BJT and (b) top face of actual BJT [8]

The manufacturers of this device were able to measure a record (at the time) current gain of $\beta=108$ in these transistors [8]. Figure 14 shows that the current gain is about 100 at room temperature (25C), and very large currents on the order of 1A are generated for base currents on

the order of 10 mA [8]. These high currents could make experimental measurements difficult because all instruments in the lab have maximum current restrictions.

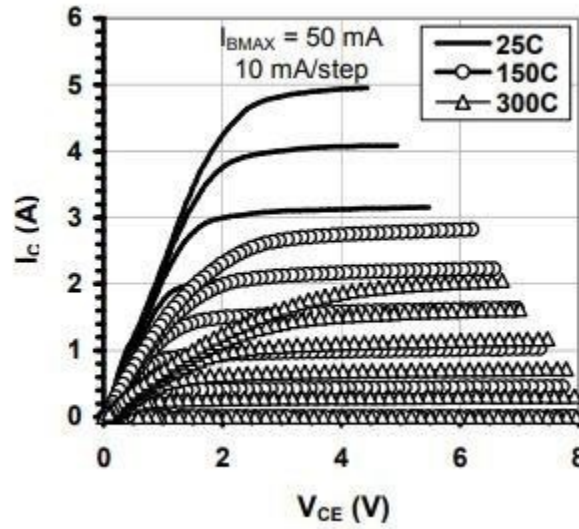


Figure 14: I-V characteristics of device used in experiments [8]

2.5 Magnetic Resonance Spectroscopy

Electron paramagnetic resonance (EPR) is a powerful technique that is used to provide information about the structure and chemical nature of electrically active defects in electronic materials and devices. Electrically detected magnetic resonance (EDMR) is a specific type of EPR that extracts a signal from a fully operational electronic device using an electronic measurement such as current. EPR and EDMR studies have identified dozens of trapping defects in semiconductors, insulators, and semiconductor/insulator interfaces in bulk materials and operational devices. This information about electrically active defects is useful for improving the performance of devices including MOSFETs, diodes, and BJTs.

2.5.1 Explanation of Electron Paramagnetic Resonance

Electron paramagnetic resonance is based on the idea that electrons can have two spin states, denoted by a spin quantum number of $m_s = +1/2$ or $-1/2$ (or spin-up and spin-down). In the absence of a magnetic field, the two spin states have the same energy, so there are an equal number of electrons in each spin state. However, when a magnetic field is applied, the energy of the two spin states deviate in energy. This is known as Zeeman splitting, and it happens because the electrons will either orient parallel to the magnetic field (lower energy) or antiparallel of the magnetic field (higher energy) [9]. The splitting of energy between spin states increases with magnetic field as shown in Figure 15. The difference in Zeeman energy ΔE is quantified as

$$\Delta E = g\beta H$$

where $g = 2.00232$ for a free electron, β is the Bohr magneton, and H is the magnetic field value. Under an applied magnetic field, the majority of unpaired electrons will occupy the lower energy spin state.

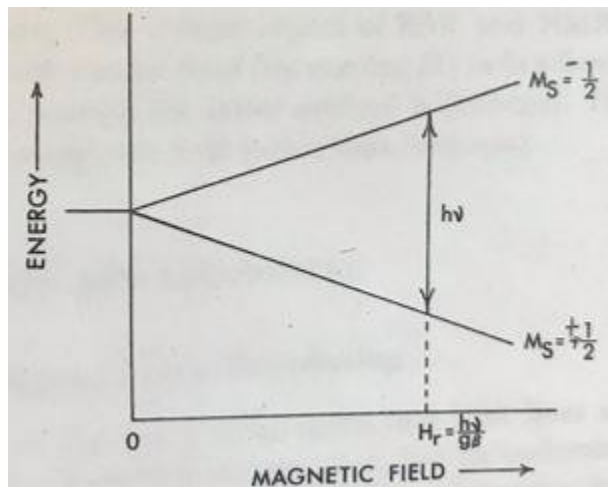


Figure 15: Zeeman splitting of electron spin state energy [13]

The basic setup for EPR is to apply a linearly varying magnetic field to a sample in one direction, and apply an electromagnetic radiation signal at a fixed frequency perpendicular to the

quasi-static field. At a certain value of magnetic field, the Zeeman energy of the electron spin states will be equal to the energy of the electromagnetic radiation, given by the Planck-Einstein equation $\Delta E = h\nu$, and the electron will absorb the energy and flip its spin. The condition for the flipping of spins is the resonance condition and it is described by the equation

$$h\nu = g\beta H$$

where h is Planck's constant (6.625×10^{-34} J-s) and ν is the fixed-field frequency (usually in the microwave range). This response due to electrons flipping spins can be plotted versus magnetic field to give the EPR signal. EPR is only sensitive to defects with an odd number of unpaired electrons because electrons that are paired together must have opposite spins by the Pauli-Exclusion Principle, so flipping their spins at resonance does not change anything.

Assuming no other magnetic fields are present around an electron, the equation above will always be true for a g value of 2.0023. However, there are always local fields around an electrically located at a defect that cause deviations from this condition. One cause of deviation from the free electron condition is called spin-orbit coupling, which is due to the movement of electrons around a charged nucleus [9]. Although it is not true, we can consider that the electron orbits around the nucleus in a circular path. From the point of view of the electron, the positively charged nucleus is orbiting around it. This movement of charge in a loop induces a magnetic field which is felt by the electron. This induced magnetic field changes the field that the electron experiences, which changes the field at which resonance occurs. This deviation from the free electron resonance condition is absorbed by the g value. The values for h , β , microwave frequency ν , and magnetic field H at resonance are all known, so the value of g for a certain defect can be found using

$$g = \frac{h\nu}{\beta H} .$$

The magnitude of the g value is different for different defects because different size atoms have different angular momentum and therefore induce different magnitude magnetic field on the electron in the defect [9]. The isotropic properties of the g value can also be measured by changing the orientation of the sample within the magnetic field. The isotropy (or anisotropy) of the g value can also reveal information about the surroundings of the electron because different hybridized orbitals have different symmetry [9]. Because of this fact, the g value is normally expressed as a second rank tensor. The g value is an important quantity that allows EPR to be used as a spectroscopic tool for identifying defects.

Other variations from the free electron resonance condition come from local magnetic fields due to magnetic nuclei. Nuclei that have an odd number of protons and neutrons will have a spin angular momentum, like an electron [13]. The spin of these nuclei create a magnetic moment, which will interact with nearby unpaired electrons. The interactions of an unpaired

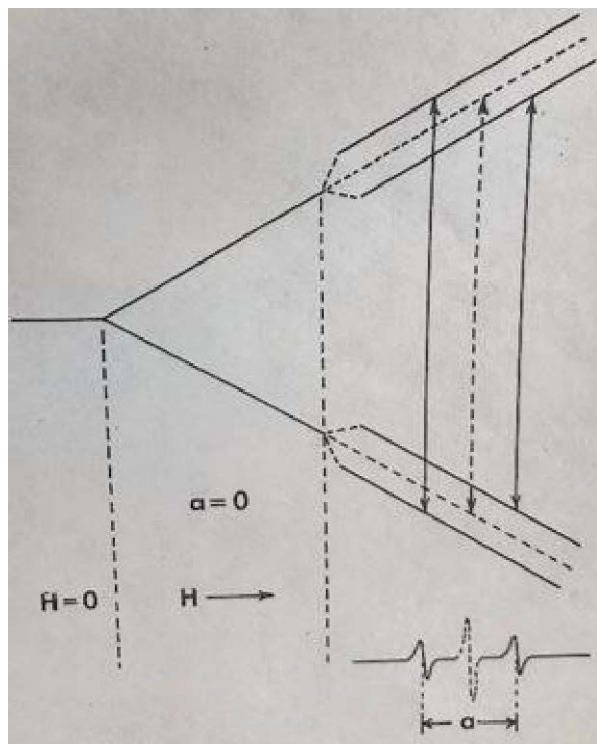


Figure 16: NHF interactions causes splitting in the resonance signal [13]

electron with nearby magnetic nuclei are called nuclear hyperfine (NHF) interactions [13]. The actual magnetic field experienced by the unpaired electron is the vector sum of the nearby nuclear magnetic moment and the external field applied. Because this sum can be additive or subtractive, NHF interactions will give rise to a “splitting” of the EPR spectrum where two peaks will be shown offset symmetrically from the main peak. Figure 16 shows that the energy of an electron spin state is changed by nearby nuclei, which cause the hyperfine splitting in the signal. The difference in the magnetic field between these two hyperfine peaks is the hyperfine coupling constant a and it is another important parameter for identifying defects. The resonance equation can be modified to account for hyperfine interactions:

$$h\nu = g\beta H + Am_I \quad (8)$$

where A is the hyperfine coupling constant, and m_I is the nuclear spin quantum number (+1/2 or -1/2) [13]. The magnitude of the hyperfine splitting can help identify the surrounding of an electrically active defect. Also, the amplitude of the hyperfine side peaks relative to the intensity of the center line should correspond to the relative abundance of magnetic nuclei of a certain element. The g value and nuclear hyperfine interactions are two important parameters that allow EPR to be used as a spectroscopic tool to identify defects semiconductors.

2.5.2 Electrically Detected Magnetic Resonance (EDMR)

Conventional EPR has a few limitations when studying semiconductor device problems. EPR is sensitive to all defects within a sample, so when studying a fabricated device, the technique will identify not only defects in the device interfaces, but also in the bulk substrate. It is not possible to identify only the defects which limit device performance. The sensitivity limit

of EPR is 10^{10} cm^{-2} , so it will not be able to detect defects in a nanoscale device if the total number of defects is less than the sensitivity limit [9]. EDMR eliminates these problems because it is more sensitive and is able to only identify defects which play a role in device performance.

One common EDMR method is spin dependent recombination (SDR). The basic idea is to use magnetic resonance to allow electrons and holes to recombine at deep-level defects. This recombination can be measured as a change in current. Figure 17, which comes from C.J. Cochrane and P.M. Lenahan [10], illustrates SDR in a p-n junction. In Figure 17a, an electron in the conduction band encounters an unpaired electron in a deep level defect. In this case, the electron and the defect electron have the same spin, which creates a triplet state between them with total spin angular momentum $S=1$. The triplet state is forbidden by the Pauli-exclusion principle (two electrons cannot occupy the same set of quantum numbers), so the triplet pair dissociates and no current is generated. In Figure 17b, the spin of the electron has been flipped because magnetic resonance has occurred, allowing it to form a singlet state ($S=0$) with the defect. Now, the free electron can recombine with a nearby hole in the valence band. This

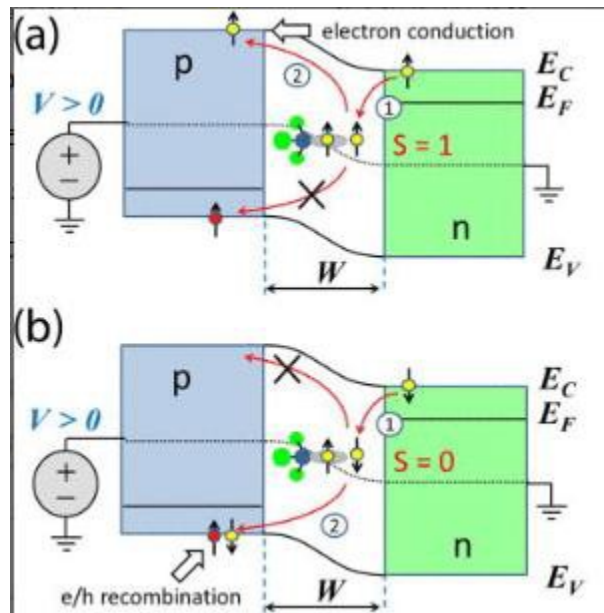


Figure 17: Spin Dependent Recombination in a p-n junction [10]

recombination generates a current, which can be measured. This process can also happen in the opposite sense when a hole in the valence band couples to a defect in the bandgap.

The application of EDMR is very similar to EPR in that a linearly varying magnetic field is applied to the device using a large magnet, and a fixed-frequency signal is applied perpendicular to the magnetic field. However, in EDMR, the sample under study is a fully operating electronic device with current running through it. At a certain value of magnetic field, resonance occurs and unpaired electrons flip their spin. This flipping of spin increases the probability of the SDR process illustrated in Figure 17. The EDMR signal displays the change in recombination current in the device due to this SDR effect versus the varying magnetic field. This signal can be analyzed in the same way an EPR signal can in order to identify recombination center defects that actually have a role in device performance.

EDMR can be conducted with different frequency oscillating magnetic fields. The most common frequency is X-band (9.5 GHz), which corresponds to a resonance field on the order of 3000G. However, more research is being done at lower fields, with frequencies on the order of 100MHz, which corresponds to resonance conditions on the order of 100G or lower. Low-field EDMR is more inexpensive than high-field EDMR, which requires very large magnets, and a lot of current to get high fields. In this lab, the low-field technique is used, as well as another technique called near zero-field magnetoresistance (NZFMR).

2.5.3 Near Zero-Field Magnetoresistance

NZFMR is a spectroscopy technique almost identical to EDMR, except that there is no applied oscillating magnetic field applied. By the definition of magnetic resonance in equation

(7), if the frequency of the oscillating field $\nu = 0$, the resonance condition cannot be met.

However, it has been demonstrated that there is an SDR response when the magnetic field B is swept through 0G. This SDR response is not caused by the same resonance effect as low-field and high-field EDMR. The physics of NZFMR is fairly complex, and not entirely understood, but a simple qualitative description is presented here.

In NZFMR, instead of transforming a triplet state to a singlet state via the flipping of electron spin, a “mixing” of singlet and triplet states occurs at low magnetic fields [10]. As mentioned previously, the magnetic field experienced by the electron at a defect is the sum of the local magnetic fields from magnetic nuclei, and the external field. As the applied field moves toward 0G, the field experienced by the electron changes, so naturally its spin orientation also changes. When an electron changes its orientation, the singlet-to-triplet ratio is modified, resulting in a change in recombination current, which gives the zero-field signal [10]. This response is heavily influenced by nearby magnetic nuclei, so NHF interactions can be observed using NZFMR [10]. Although the g -factor is no longer a useful parameter at zero-field, useful information including but not limited to NHF interactions can be observed without the need for an oscillating magnetic field. One goal of this research is to contribute to the development of NZFMR as a low cost and low energy alternative to high field EDMR as a spectroscopic tool for understanding electrically active defects in semiconductors.

2.6 Review of Past Research on EDMR in SiC BJTs

As discussed earlier, the most important parameter for a SiC BJTs is the current gain. While SiC BJTs can operate at high voltages and currents, their potential is limited by a high density of recombination centers in the base which limit the current gain. There is still very little known about the chemistry and physics of these defects. One of the first published paper about performing SDR on SiC BJTs comes from C.J Cochrane and P.M. Lenahan in 2007 [11]. The BJT used in this research was also fabricated by Cree Corporation. The authors performed SDR on the base-collector junction of the transistor based on previous research which indicated that a high density of recombination centers at this interface limits device performance. The measurements were performed at X-band frequency (9.5GHz). Their SDR response was dominated by a single, isotropic line, with no side peaks and a $g=2.0024$. They tentatively concluded that the SDR spectrum was due to a Si vacancy (the absence of a Si atom in the lattice) in its singly negatively charged state based on previous EPR data which observed a similar response in large volume SiC samples.

In another paper by Cochrane and Lenahan, they performed SDR on a different SiC BJT also fabricated by Cree [12]. In this study, 4 NHF side peaks were identified in the SDR signal with a central signal that had an isotropic g value of 2.0029. They realized that these side peaks are due to the presence of magnetic nuclei spin $\frac{1}{2}$ ^{29}Si , which is 4.67% abundant, and spin $\frac{1}{2}$ ^{13}C , which is 1.1% abundant. They concluded that the spectrum is not from just one defect, but is associated with an intrinsic aggregate defect, likely from a divacancy or carbon vacancy/antisite. A divacancy is a Si and C vacancy next to each other in the lattice, and an antisite is when a Si atom occupies a C site in the lattice or vice versa. The authors were able to create a first order model of the possible arrangements of magnetic nuclei around these two defects, and how these

arrangements would affect the SDR response. Their theoretical model supported their experimental research, which led to the tentative assignment of either a divacancy or vacancy/antisite. This SDR response was different than their previous work which identified a silicon vacancy as the dominating defect.

Another important behavior of the SiC pn junction that Cochrane and Lenahan discovered in their research was the SDR response to varying junction biases. The recombination current in the space charge of a p-n junction can be described by an equation, assuming a uniform distribution of trapping centers [11]. The equation is

$$J_r = \frac{qn_i W}{2} v_{th} N_t \sigma \exp\left(\frac{qV_a}{2kT}\right),$$

where v_{th} is the thermal velocity, N_t is the density of recombination defects, σ is the capture cross section of the defect, n_i is the intrinsic carrier concentration of 4H-SiC ($\sim 5 \times 10^{-9} \text{ cm}^{-3}$), V_a is the junction bias, and W is the width of the depletion region. The width of the depletion region is given by the equation

$$W = \left[\frac{2\epsilon(N_a + N_d)(V_{bi} - V_a)}{qN_a N_d} \right]^{1/2},$$

where N_a is the density of ionized acceptors, N_d is the density of ionized donors, and V_{bi} is the built-in voltage, defined as

$$V_{bi} = \frac{kT}{q} \ln\left(\frac{N_a N_d}{n_i^2}\right).$$

The authors plotted J_r over junction bias, which has a thin peak between 2.5 and 3V, as shown in the figure below [11]. They were able to show a distinct qualitative relation between the SDR response amplitude versus voltage bias and the theoretical recombination current over junction

voltage. This qualitative relationship shows that the SDR response is directly related to the recombination current in the space charge region, which is where we want to examine performance limiting defects. This fact validates the theory of SDR. This also means that there is a fairly small range of junction bias for which a large SDR response will be achieved, which must be taken into account during the EDMR experiment. The slight quantitative variation

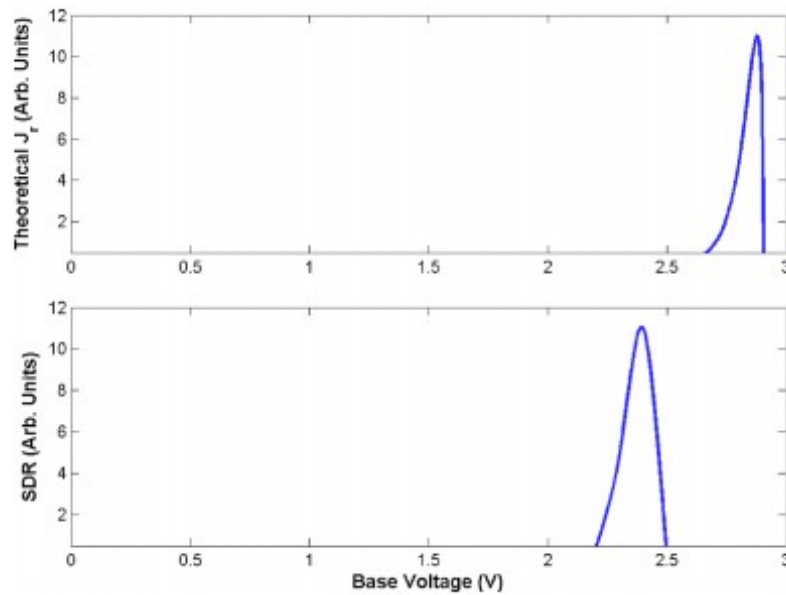


Figure 18: a) Theoretical recombination current and b) SDR amplitude [11]

between the theoretical J_r and the actual SDR response is expected because of simplifications made in the theoretical calculations, as well as the fact that the distribution of trapping centers is likely not uniform.

In another paper by Cochrane and Lenahan, they use NZFMR to demonstrate an SDR response in a SiC diode in the absence of a secondary oscillating magnetic field. In a low-field SDR measurement with an oscillating RF field of 200MHz applied, there were two signals centered at ± 71 G, which was expected, along with a signal at 0G, which is not normally expected [10]. The fully saturated resonant signal was about 2.35 times as large as the zero-field signal [10]. Multiple hyperfine peaks are apparent in this signal. The authors also performed

NZFMR, where there was not oscillating field, and there is still a signal at 0G. They compared the hyperfine peaks present in the ZF signal with the high-field response at X-band (9.5GHz, 3394G). Their comparison showed that each side peak present in the high field signal has a similar corresponding peak in the zero fields signal. The spectrum is not exactly the same, however that is expected for several reasons. One reason for this shift is that the orientation of magnetic nuclei will not be the same at high and low field, because at high field the magnetic field experienced by the nuclei is more dominated by the applied field, and at low field it is more dominated by the magnetic field of the nearby unpaired electron [10]. Therefore, resonance will occur at a different field relative to the center of the signal. This discovery of symmetrical and predictable hyperfine interactions at different field strengths could allow for direct correlation with other hyperfine patterns that are better-understood. Because the response with zero applied oscillating field is similar to the high-field signal, it is possible for low and zero-field magnetic resonance spectroscopy to be used as a lower cost alternative to high field magnetic resonance spectroscopy.

The SiC used in this study is of extremely high purity, except for the dopant atoms which are nitrogen (N) and aluminum (Al). N and Al both have 100% abundant magnetic nuclei, while the ^{29}Si and ^{13}C nuclei present in the SiC have magnetic nuclei concentrations of only 4.67% and 1.1%, respectively [12]. These differences in concentration will be taken into account when identifying hyperfine interactions because the modest abundance of Si and C magnetic nuclei will have a different effect than N and Al. Many intrinsic defects in bulk SiC have been identified in conventional EPR studies [16-27]. The EPR and EDMR responses in literature can be compared with the low-field and zero-field SDR responses found in the Chapter 4.

2.6.1 SiC p-n Junctions as Deep Space Magnetometers

One relevant application of the research in this paper is for a solid state magnetometer that can be used in space exploration missions. Magnetic field measurements have been used in space missions in order to understand many aspects of planetary objects including understanding planetary atmospheres and their ability to harbor life, as well as the presence of water [15]. For example in 1996, the magnetometer aboard the Galileo spacecraft gathered data from Jupiter's moon Europa that suggested the presence of water beneath the surface ice sheet [15]. Another mission to Europa is planned for the 2020s which will further explore the existence of water on the moon. The magnetometers commonly used in space exploration missions are very complex, large and costly. However, C.J. Cochrane *et al.* [15] designed a solid-state magnetometer which is based on a 4H-SiC p-n junction, like the one studied in this paper. The magnetometer measures changes in currents caused by the interaction of external magnetic fields and atomic-scale defects on a 4H-SiC p-n junction [15]. The thermal properties of 4H-SiC and its resistance to radiation damage make it a suitable material for the harsh environment in outer space.

The sensor works using the phenomenon of NZFMR discussed earlier in this paper. The effectiveness of a magnetometer is based on how sensitive it is to very small magnetic field changes. As discussed earlier, near-zero magnetic fields can cause changes in recombination current in a solid-state device by a mixing of singlet and triplet defect states. If the NZFMR response of the SiC p-n junction is well understood, changes in recombination current can be measured and used to determine the corresponding change in magnetic field. The sensitivity is determined by the following equation given by Cochrane *et. Al* [15]:

$$sensitivity = \frac{\delta B}{\sqrt{\Delta f}} = 2\sigma \sqrt{\pi q} \frac{\sqrt{t_0}}{\Delta l} \left(\frac{T}{\sqrt{Hz}} \right)$$

where σ is the width of the NZFMR signal in tesla (T), q is the elementary charge, I_0 is the DC current passing through the device, and ΔI is the magnitude of the change in recombination current at zero magnetic field. The sensitivity is expressed as the uncertainty in the magnetic field δB normalized over the square root of the bandwidth of the measurement Δf in units of $T/Hz^{-1/2}$. The sensitivity of the base-collector junction of the 4H-SiC BJT studied in this paper can be determined through NZFMR measurements and compared to other SiC p-n junction devices.

Chapter 3

Experimental Methods

3.1 EDMR Spectrometers

The EDMR data was taken on 3 different spectrometers, which were essentially custom-built and have the same basic setup. A simple schematic of the components involved in this system is shown in Figure 19. The electromagnet consisted of a series of four sets of Helmholtz coils with increasing radii which provide a uniform DC magnetic field signal. The magnetic field applied to the signal by the electromagnet is controlled by a magnet power supply which is programmed by the PI controller in the computer. A hall probe is used to monitor the DC field, which sends data to the computer in order to accurately control the linearly varying magnetic field. The electromagnet is typically operated in the range of $\pm 200\text{G}$. This is a much smaller field

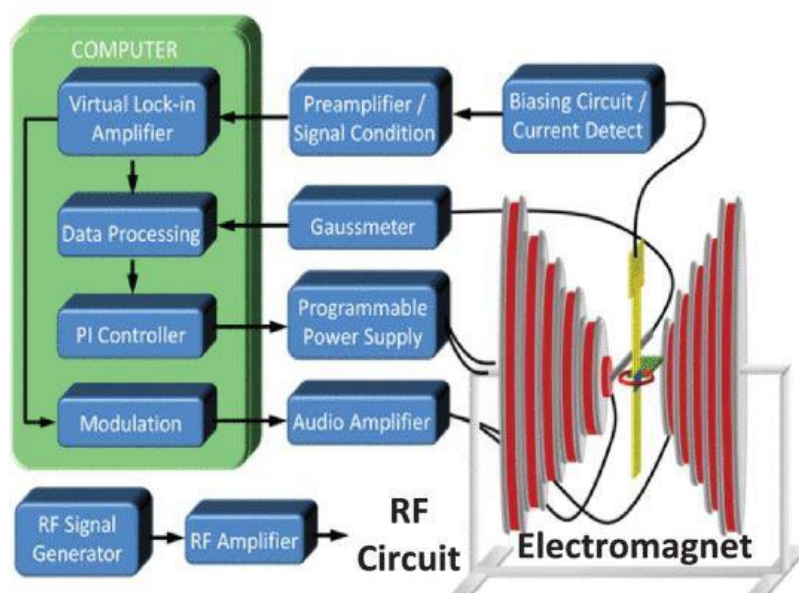


Figure 19: Schematic of Low-Field EDMR Spectrometer [5]

than a high-field magnetic (range of 3000G), and therefore the low-field electromagnets do not require elaborate and expensive cooling mechanisms. The low-field electromagnets also require much less current to generate the necessary magnetic fields, which means they take less energy to run.

In addition to the four sets of Helmholtz coils for the DC magnetic field, there is also 1 set of smaller Helmholtz coils that are used to apply a frequency modulated magnetic field. This modulated magnetic field is important in order to improve the signal-to-noise ratio of EDMR signals. This AC magnetic field is modulated at a frequency on the order of 1-10kHz, and an amplitude around 1-10G. This means that as the DC magnetic field increases linearly, there is an overlapped AC signal. The EDMR response from the device will oscillate at this same frequency and phase. This oscillating signal is passed into a frequency-sensitive lock-in amplifier which filters out any signals not in the specified bandwidth, and therefore filters out noise and amplifies the signal. It is important to note that the modulated signal will only detect features in the signal that are greater than or equal to the modulation amplitude, and it will broaden smaller features to be the same size as the modulation amplitude. This means that smaller modulation amplitudes are desired for detecting small features in the signal. However, decreasing the modulation amplitude will also increase the noise. The modulation frequency used in this lab was 1100Hz, and the modulation amplitude varied between 1G and 5G. The signal displayed on the computer software is actually a first derivative of the change in recombination current in the device.

Two other important components of the spectrometer are the preamplifier and the biasing circuit. The first spectrometer used in the experiment was a custom built Blue Spin spectrometer which has a custom preamplifier that consists of a current to voltage converter with 5 coarse gain settings and five fine gain settings, a high pass and low pass filter, and a built in biasing circuit.

The biasing circuit allows the user to move around jumpers in a biasing matrix to apply bias, ground or virtual ground the necessary terminals of the device. The other two spectrometers (2 and 2) used in this research had a Stanford preamplifier which was used as a current to voltage converter and high pass filter. With these spectrometers a custom-built VNC to USB cable was used to bias the device directly from the power supply on the preamp. This cable was designed so that only two leads of the device would be connected together, with the third lead floating.

In the low-field EDMR measurements, an RF signal generator was used to control the RF oscillating magnetic field perpendicular to the quasi-static linearly varying magnetic field. The RF signal is sent to an RF coil which the device is placed within. In this experiment, the oscillating field was at a frequency of 151MHz. The RF circuit was not used in NZFMR measurements.

3.2 Procedure

The first step of the process was to mount the device to a “T,” which has a USB port that was used to apply a bias to the device. The device was placed with the collector side facing down, with electric paint between the collector and a metal pad to create a conductive contact. Elmer’s glue was placed on the side of the device to hold it in place. After the paint and the glue dried, a wire bonder was used to make contact to the base and emitter. The “T” was then housed in a test tube, to avoid damaging the fragile wire bonds.

Before conducting EDMR experiments, the current and voltage characteristics of the device were studied using a Semiconductor Parametric Analyzer (SPA). The base-collector diode and emitter-base diode were each studied separately without the third lead connected in order to

look at the current vs. voltage diode curves of the two p-n junctions. In each case, the voltage on one terminal was swept from 0V to 3V, while the other terminal was grounded, so as to apply a forward bias to the junction. The current through the junction was measured as a function of voltage.

Then, the BJT was biased in the common-emitter configuration to look at the forward characteristics of the device. In this configuration, the emitter was grounded, a constant current was applied to the base, and the base-collector junction was reverse bias. In this measurement, the base current was stepped in 5mA increments starting at 0mA, while the collector voltage was swept from 0V to 5V for each base current. The current through the emitter and collector were measured and recorded by the SPA, and the results were plotted. This measurement was done to see how well the device used in this paper matched the device discussed in section 2.4.1, whose characteristic curves are shown in Figure 14 in that section.

After the SPA measurements were performed to understand the current and voltage characteristics of the device, the SDR experiments were performed. The details of the instruments used for SDR are discussed in section 3.1. Almost all of the SDR measurements were performed on the base-collector junction of the BJT, which is the junction that most literature in this area has investigated. The first experiment was to determine the forward bias voltage that resulted in the largest SDR signal amplitude. For this experiment, NZFMR was performed on spectrometer 1 and the RF circuit was not used. The SDR signal produced by the spectrometer on the computer is the first derivative of the change in recombination current ΔI in the device over the applied field. However, the amplitude of the signal on the computer is not the best indication of the signal strength because as the DC base current I_B increases due to the forward bias increasing, the magnitude of the change in recombination current will also increase

simply because there are more charge carriers flowing. It is ideal to have a signal where the ratio of the amplitude of the change in recombination current to the magnitude of the DC base current is largest. The higher this ratio is, the more sensitive the SDR signal is which makes it easier to peak up NHF patterns that might otherwise get drowned out by noise. Therefore, the SDR signal amplitude is expressed as the ratio $\Delta I/I_B$. In order to maximize this value, NZFMR was performed at 5 different forward biases between 2.3V and 2.6V. At each forward bias, the value of the DC base current I_B was recorded. For each measurement, the same spectrometer settings were used, and the signal was averaged over 15 scans. After 15 scans the amplitude of the ΔI plot on the computer was recorded and divided by I_B to get the SDR signal amplitude.

Once the ideal forward bias was determined, a NZFMR measurement was taken for almost 60 hours in order to signal average for a long time to increase the signal to noise ratio as much as possible. The modulation amplitude was 2.5G, the modulation frequency was 1100Hz, the RC time constant was 0.3s, the sweep width was 100G, and the sweep time was 60 seconds per scan. The signal was averaged for 3572. A second NZFMR measurement was taken using a second spectrometer. The same settings were used as the first measurements. The second spectrometer has a built-in software filter that reduces noise in the signal and is meant to amplify hyperfine side peaks that might be drowned out by noise. The signal was averaged over 1286 scans for 21.4 hours. Another NZFMR measurement was taken on a third spectrometer with the same spectrometer settings, and the signal was averaged for 30 hours over 1784 scans.

In addition to the NZFMR measurements which were taken without the presence of an oscillating magnetic field, SDR measurements were taken on the base-collector junction of the 4H-SiC BJT using spectrometer 2 with an applied oscillating magnetic field of frequency of $\nu=151\text{MHz}$. These oscillating field was applied using the RF circuit discussed in section 3.1. A

wide scan was taken with a sweep width of 200G, modulation amplitude of 3.5G, modulation frequency of 1100Hz, and a time constant of 0.3s. The signal was averaged over 917 scans for 16 hours.

In order to further investigate the low-field SDR signal, three more SDR measurements were taken on the base-collector junction with the applied RF oscillating field of frequency 151MHz. These scans were 100 G wide (from -110G to 10G) with a modulation amplitude of 3.5G. The device orientation was rotated 45 degrees between each of the scans in order to investigate the isotropy of the signal.

Finally, SDR measurements were attempted on the base-emitter junction of the BJT at various forward biases. However, as discussed in section 4.6, no SDR signal was ever found.

Chapter 4

Results and Discussion

4.1 SPA Measurements

The I-V curves of the emitter-base junction and base-collector junction are plotted in Figure 20 on the same axis. The emitter-base current was much higher than the base-collector current until about -2.6V. The emitter is always more heavily doped than the collector, so there

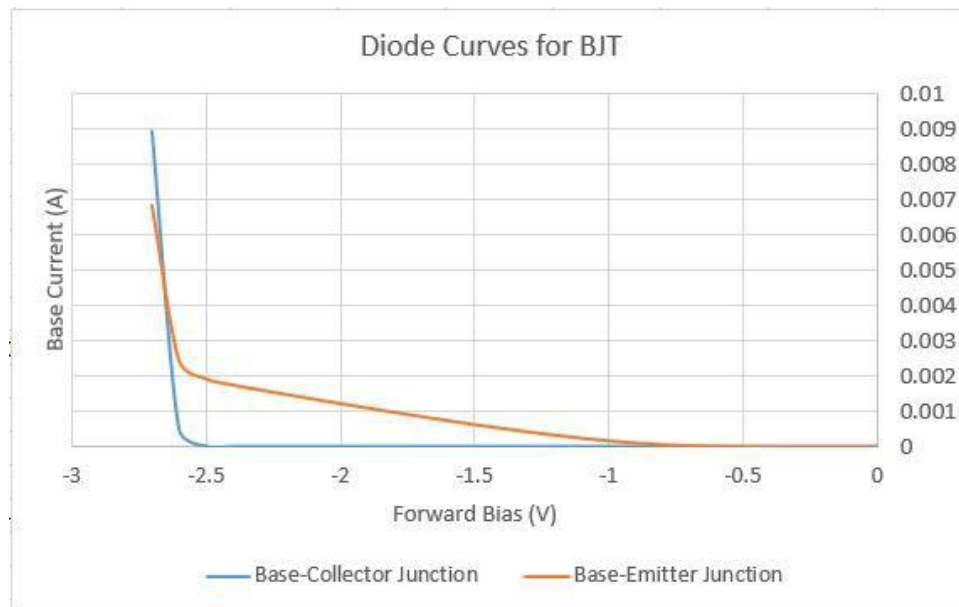


Figure 20: I-V Curves for BJT junctions

should be more current in the emitter-base junction. The base-collector junction is a more ideal I-V curve for a p-n junction with almost no current until a certain voltage (~ -2.5 V) when the current increases sharply. However, the current in the emitter-base junction is increasingly steadily starting at 0V. This high current at low voltages in the emitter base-junction is alarming for EDMR measurements on this junction because it is very hard to measure a change in

recombination current in the base when the DC current going through the base is so large.

Luckily, the base-collector junction is still of interest for SDR measurements.

The second set of curves taken using the SPA was the common-emitter forward characteristic curves shown in Figure 20. The base current was stepped in 5mA increments to get 8 different curves. The shape of the curves is consistent with BJT behavior discussed earlier in this paper. However, these curves do not quantitatively match the common-emitter curves for the device in literature in Figure 14. The gain β of the BJT should be close to 100, however in these curves the highest β value is 1.6, which is not a reasonable gain for a BJT. If the base current is on the order of 10^{-2} A, the collector current should be on the order of 1 A. The device does show the qualitative properties of a BJT, which is promising, however the gain is very poor. However, the poor performance of the device could actually be beneficial in the SDR measurements because it could mean there is a higher density of defects which will lead to robust SDR signals.

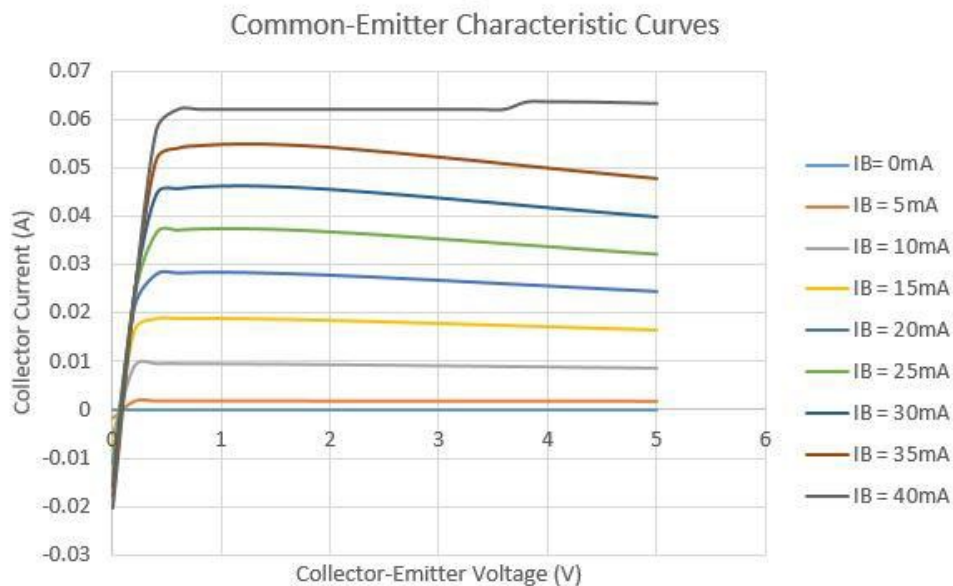


Figure 21: Common-emitter characteristic curves

4.2 Validation of SDR Response

Several SDR measurements were done on the base-collector junction of the BJT. First, the ideal forward bias was determined by measuring the NZFMR signal amplitude at several different forward bias voltages. Table 2 shows the results from NZFMR signals at 5 different forward bias values. Recall that the actual SDR signal amplitude is determined by the ratio of the change in recombination current ΔI to the total DC current passing through the junction I . The ideal forward bias voltage was determined to be 2.45V, which is the bias that was used for all the signals taken in the remainder of this paper. Figure 22 shows the relationship between NZFMR signal amplitude and forward bias. This graph qualitatively matches the theoretical plot of recombination current vs voltage in a p-n junction as discussed in section 2.6, shown in Figure 23 for the device studied in this lab. The recombination current in the depletion region of a p-n junction can be described by an equation, assuming a uniform distribution of trapping centers [11]. The equation is

$$J_r = \frac{qn_i W}{2} v_{th} N_t \sigma \exp\left(\frac{qV_a}{2kT}\right),$$

where v_{th} is the thermal velocity, N_t is the density of recombination defects, σ is the capture cross section of the defect, n_i is the intrinsic carrier concentration of 4H-SiC ($\sim 5 \times 10^{-9} \text{ cm}^{-3}$), V_a is the junction bias, and W is the width of the depletion region. The width of the depletion region is given by the equation

$$W = \left[\frac{2\epsilon(N_a + N_d)(V_{bi} - V_a)}{qN_a N_d} \right]^{1/2},$$

where N_a is the density of ionized acceptors, N_d is the density of ionized donors, and V_{bi} is the built-in voltage, defined as

$$V_{bi} = \frac{kT}{q} \ln\left(\frac{N_a N_d}{n_i^2}\right).$$

Table 2: NZFMR signal amplitude at different forward bias voltages

Forward Bias (V)	I_B (μ A)	ΔI (pA)	Signal Amplitude $\Delta I/I_B$ (arb. Units)
2.3	0.0684	no signal	0
2.4	0.778	3.1	3.98
2.45	2.93	15.12	5.16
2.5	15	47	3.1
2.6	487	40	0.082

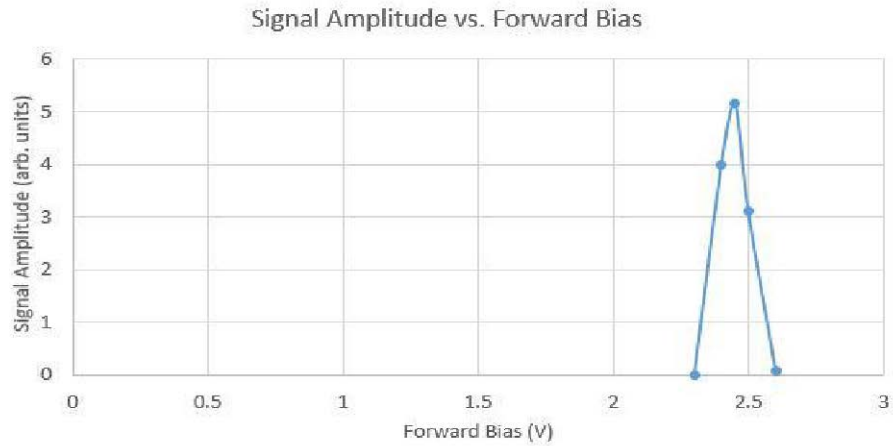


Figure 22: NZFMR signal amplitude versus forward bias voltage

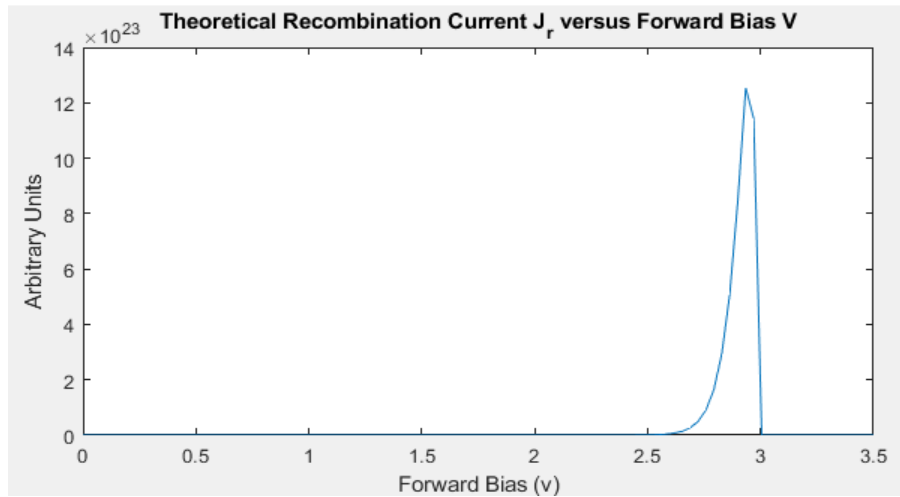


Figure 23: Theoretical relationship between recombination current and forward bias in the 4H-SiC pn junction

Not all of the constants in these equations were readily available for the device used in this lab, but it was possible to still plot a more qualitative graph of the recombination current J_r by absorbing many constants into a single constant to get the following equation [10]:

$$J_r = C\sqrt{V_{bi} - V_a} * \exp\left(\frac{qV_a}{2kT}\right), \text{ for } V_{bi} > V_a,$$

where C is a constant. This equation will give the same shape of the plot, only the units of current will be arbitrary. The MATLAB code to generate the plot of J_r shown in Figure 23 versus forward bias can be found in the Appendix.

The shape of the graphs in Figures 22 and 23 are qualitatively very similar. The width of the region with the best signal amplitude in Figure 22 has is about 0.3V, which is about the same as the width of the region where recombination current is the highest in Figure 23. The quantitative discrepancy in voltage in the two graphs is reasonable considering the recombination current equation makes many assumptions including that the density of recombination centers is uniform throughout the depletion region, which is unlikely. This qualitative agreement between recombination current and NZFMR signal amplitude proves that the NZFMR response is dominated by recombination current, and that the defects responsible for the signal are in fact recombination centers in the depletion region of the pn junction.

4.3 NZFMR on Base-Collector Junction Results

Once the ideal forward bias was determined, a NZFMR measurement was taken using the first spectrometer. The signal was averaged for 60 hours over 3572 scans and is shown in Figure 24. Recall that the signal displayed on the spectrometer software is actually a first derivative of the change in recombination current. Therefore, the derivative of this signal is referred to as the second derivative. The signal to noise ratio (SNR) in this signal is very low, but some noise is still present. There are no obvious NHF side peaks, which is discouraging. However, as shown in figure 24, there are seemingly two sets of very small peaks spaced almost symmetrically from

the center line at around $\pm 11\text{G}$ and $\pm 33\text{G}$. Hyperfine peaks are usually more pronounced in the second derivative signal which is shown in figure 25. Although there are slight peaks in the same location as figure 24, these peaks are not as large as usual hyperfine peaks and these peaks are

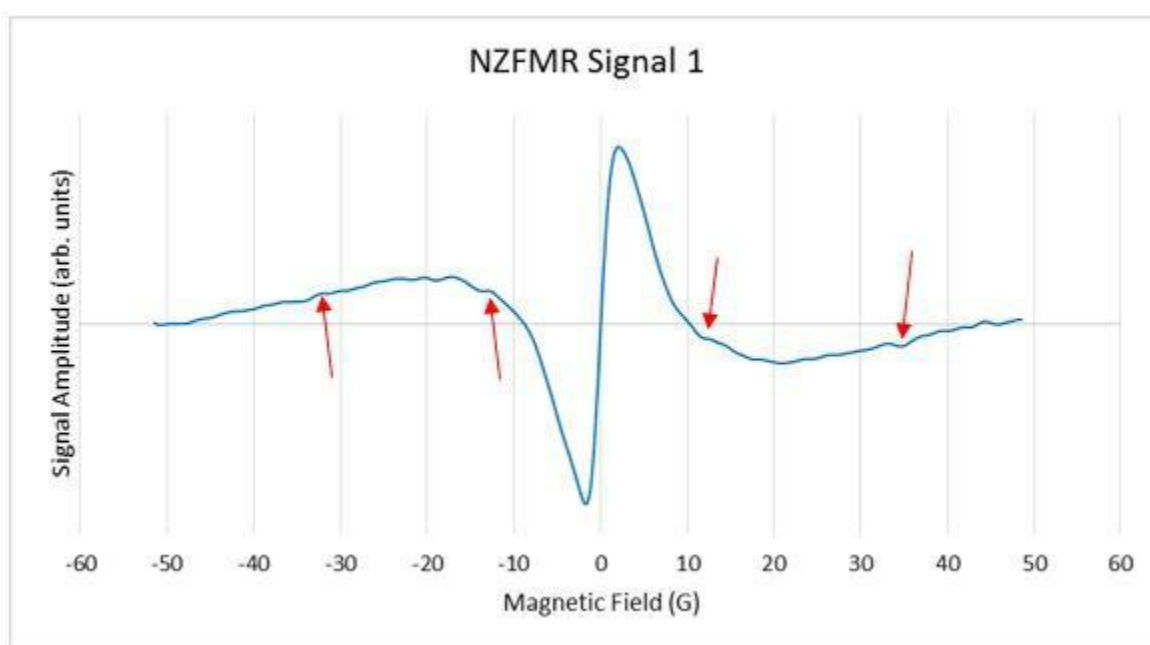


Figure 25: First NZFMR signal, averaged over 3572 scans

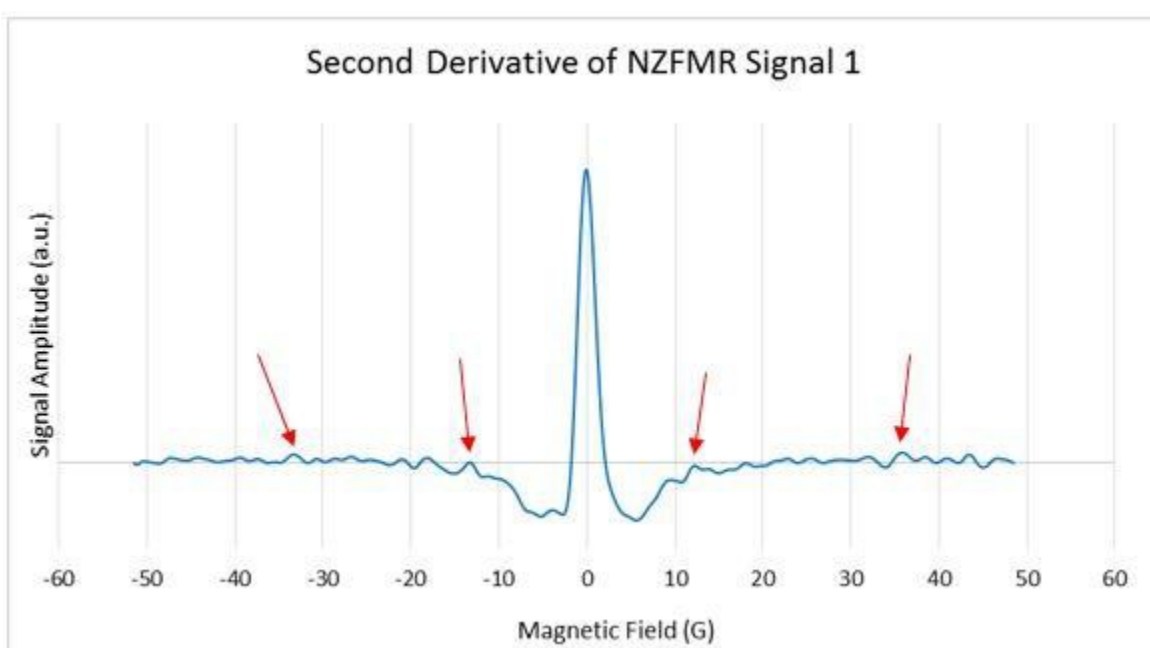


Figure 24: Second Derivative of NZFMR Signal 1

not very much larger than the noise. Therefore it is not reasonable to conclude that these are NHF peaks simply based on this one signal.

In order to investigate the possibility of NHF peaks in the first zero field signal, three more NZFMR measurements were taken on the same device. The second signal was taken using a different spectrometer than the first in order to investigate if the slight peaks from the first signal were repeatable. The signal was averaged over 1286 scans for 21.4 hours. The second NZFMR signal and its derivative are shown in Figures 26 and 27, respectively. The SNR is about as good as the first signal in a third of the scans mainly because of the software filter. However, there is very little evidence of hyperfine peaks. The one noticeable peak is around -30G, which is similar to a feature in the first scan, however there is no symmetrical peak at +30G. The second derivative in Figure 27 also shows no evidence of any hyperfine peaks.

The third signal was taken on a third spectrometer and it is shown in Figure 28. The signal is a bit noisier than the previous signal, however there are some wiggles indicated in Figure 28, which seem promising. The wiggles are located around ± 11 G, which is the same as in the first scan. However, these features are barely distinguishable from the noise in the derivative shown in Figure 29. Again, it is not reasonable to conclude that these are indeed NHF peaks, although it is slightly reassuring that a similar pattern has occurred in two separate signals on different spectrometers.

In order to attempt to get a signal with fully-defined NHF peaks, the device was placed back into the first spectrometer used, and the spectrometer settings were adjusted to find the best SNR ratio. The modulation amplitude was adjusted between 1G, 2.5G, and 3.5G, and the RC time constant was adjusted between 0.1s, 0.3s, and 0.6s. Ideally, it would be best to have the lowest possible modulation amplitude, with the least possible noise, however 1G modulation

always resulted in noisy signals that would take days to bring down to a reasonable level.

Different settings were tested and the signals were averaged over the same amount of time (about 20 minutes) and the SNR was measured each time. It turned out that the best SNR was given by the settings that were used in the first three scans: 2.5G modulation amplitude, and time constant of 0.3s. Unfortunately, in the many scans attempted, no hyperfine peaks were ever resolved, and the signal noise was still too overwhelming. A fourth NZFMR signal and its derivative are shown in Figures 30 and 31. This signal was averaged for 19 hours over 1150 scans. The peaks at $\pm 11\text{G}$ are not obvious, which further diminishes the possibility that they are indeed hyperfine side peaks. It is worth noting that NHF side peaks with splitting of $\pm 11\text{G}$ have been identified in a high-field EDMR measurement in a 4H-SiC pn-junction which is linked to an aggregate defect consisting of either a divacancy or a carbon vacancy/antisite [12]. However, these hyperfine peaks were accompanied by three other sets of hyperfine peaks, which are not distinguishable in any of the four signals in this paper.

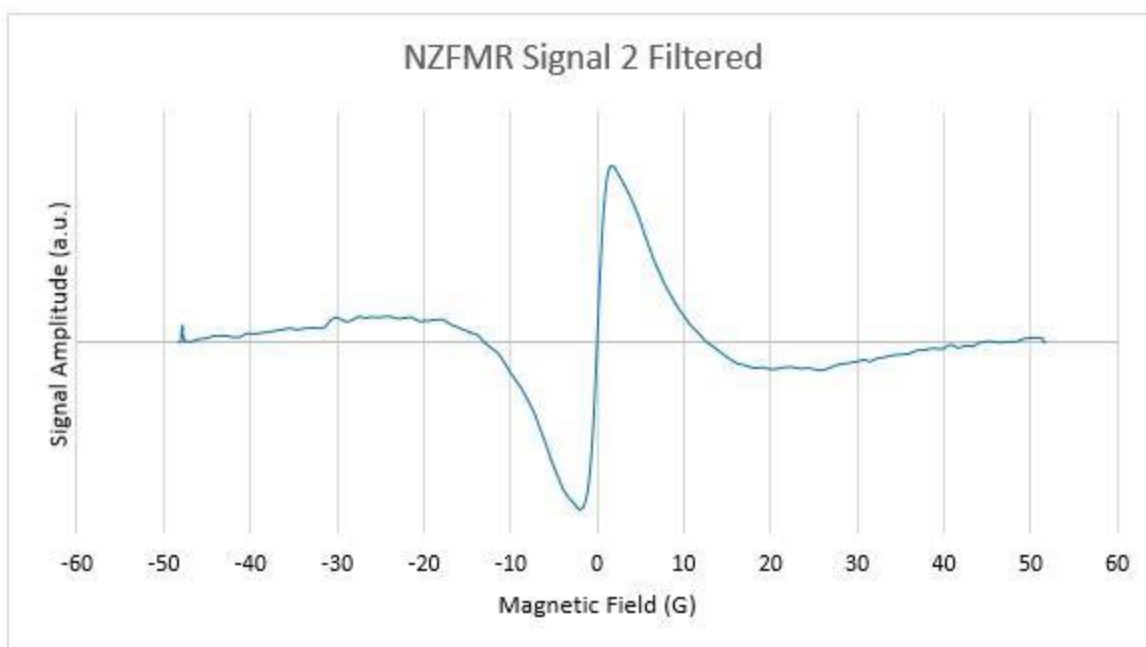


Figure 26: NZFMR Signal 2 using spectrometer 2

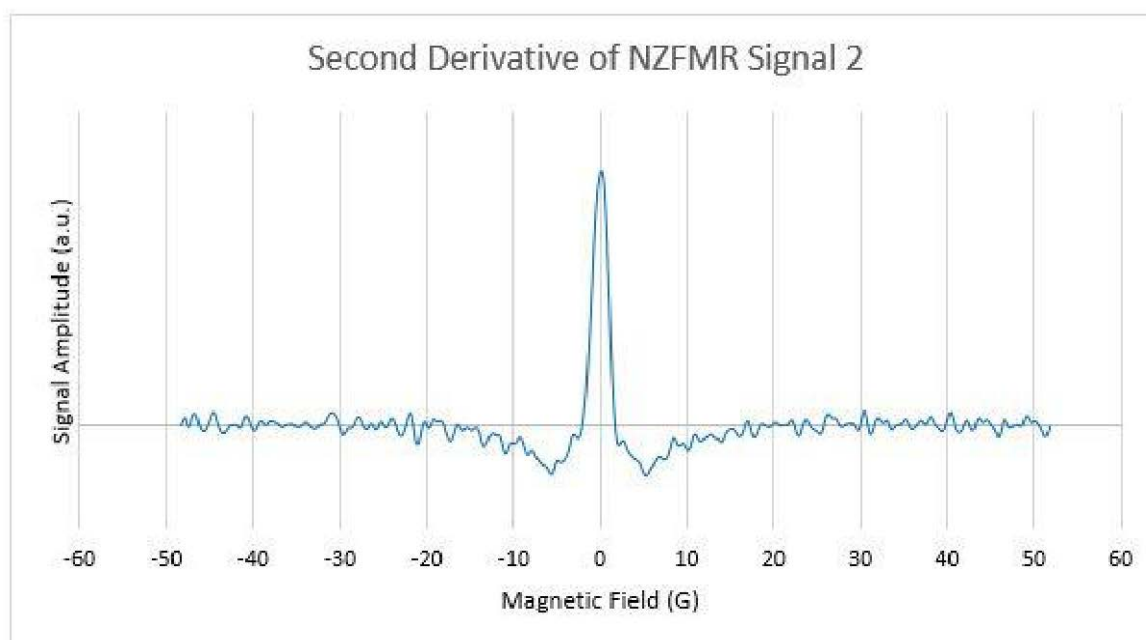


Figure 27: Second derivative of NZFMR signal 2

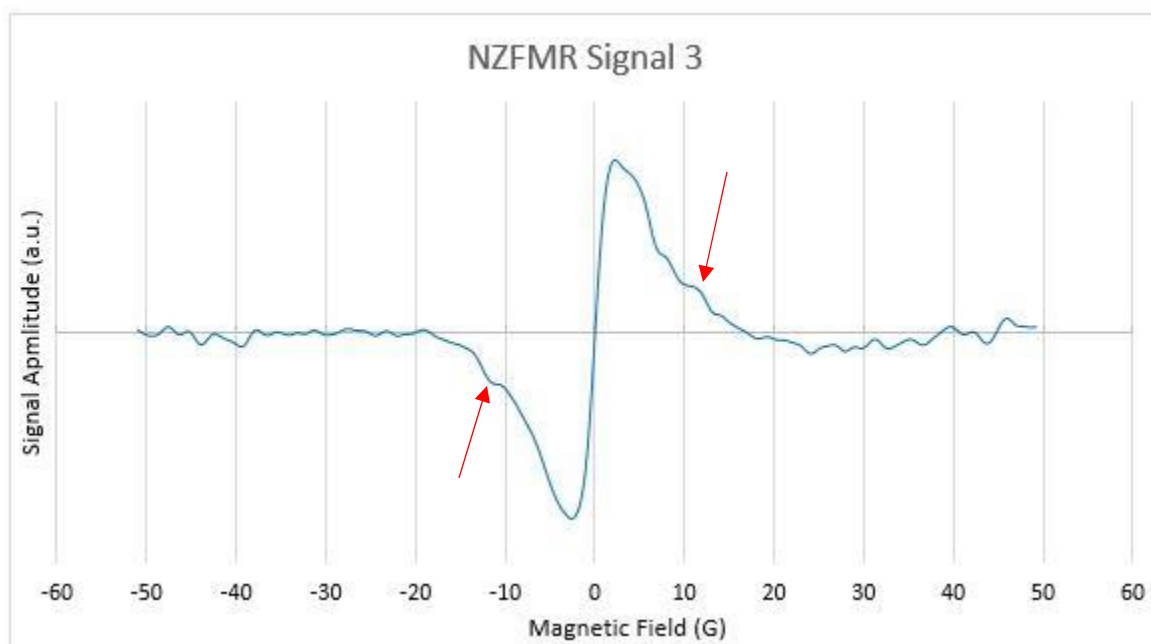


Figure 28: NZFMR signal 3 using spectrometer 3

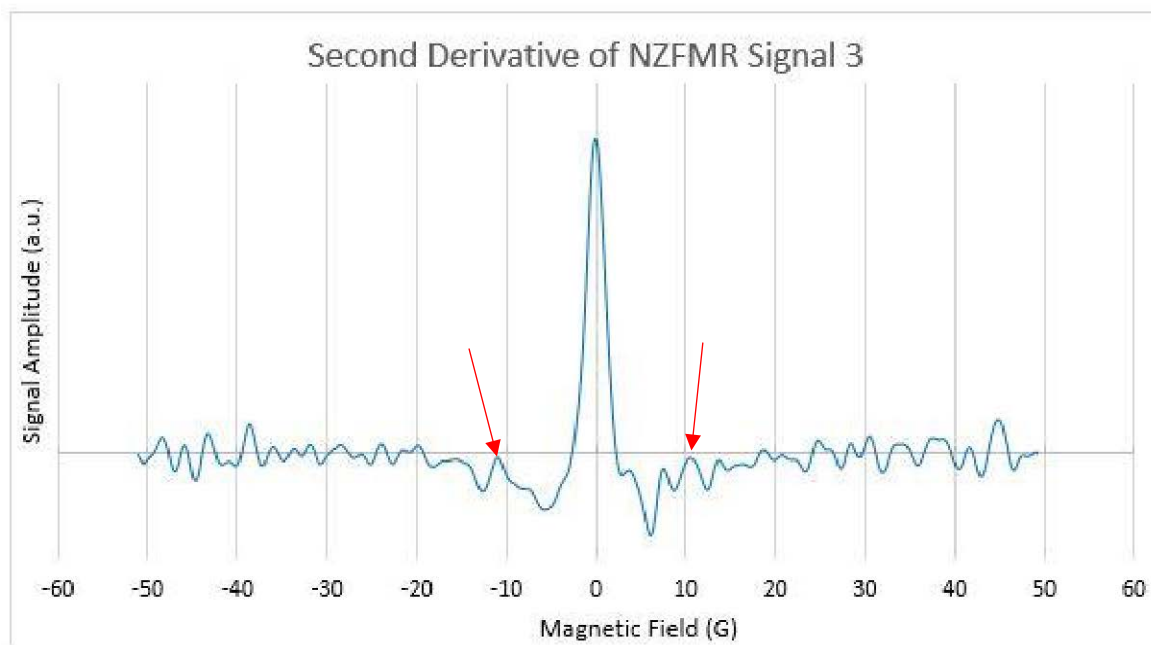


Figure 29: Derivative of NZFMR signal 3

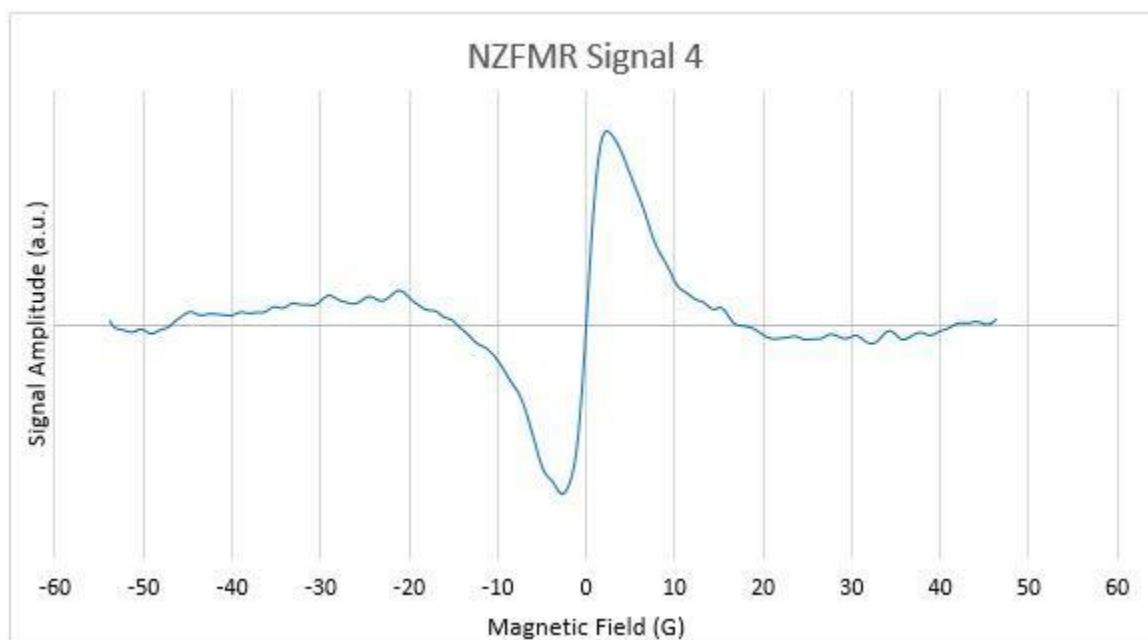


Figure 30: NZFMR Signal 4 using first spectrometer

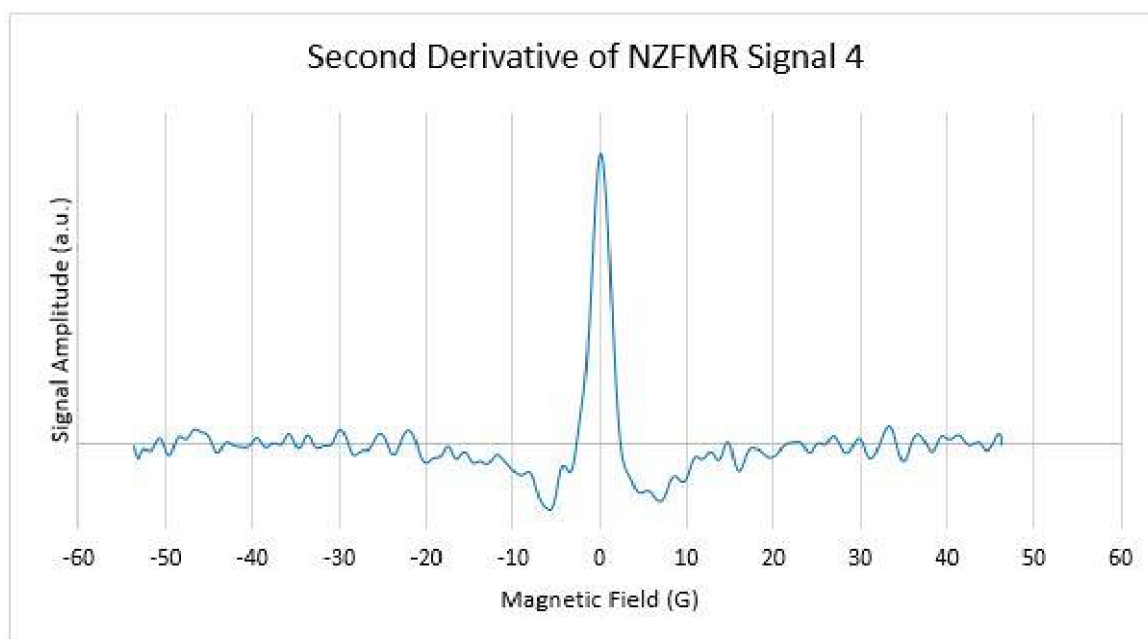


Figure 31: Derivative of NZFMR Signal 4

4.4 Magnetometer Sensitivity of the Base-Collector Junction

Although the NZFMR signals did not indicate the presence of NHF peaks, the signals can still be analyzed in terms of the deep space magnetometer application discussed in Section 2.6.1. The sensitivity of a deep space magnetometer based on a SiC p-n junction can be determined by the following equation given by Cochrane *et. Al* [15]:

$$sensitivity = \frac{\delta B}{\sqrt{\Delta f}} = 2\sigma \sqrt{\pi q} \frac{\sqrt{I_0}}{\Delta I} \left(\frac{T}{\sqrt{Hz}} \right)$$

where σ is the width of the NZFMR signal in tesla (T), q is the elementary charge, I_0 is the DC current passing through the device, and ΔI is the magnitude of the change in recombination current at zero magnetic field. The sensitivity is expressed as the uncertainty in the magnetic field δB normalized over the square root of the bandwidth of the measurement Δf in units of $T/Hz^{1/2}$.

All the necessary parameters are known from the NZFMR signals discussed in section 4.2. Table 3 show the necessary parameters for all four of the NZFMR signals and the corresponding sensitivity values. The ideal p-n junction for the deep space magnetometer will

Table 3: Magnetometer sensitivity of the four NZFMR signals

	Signal Width σ (T)	DC Current I_0 (A)	Change in Recombination Current ΔI (A)	Sensitivity ($T/Hz^{1/2}$)
Signal 1	3.96E-4	3E-6	5.33E-12	1.82E-4
Signal 2	3.76E-4	3E-6	1.79E-11	5.16E-5
Signal 3	4.92E-4	2.93E-6	1.79E-11	6.70E-5
Signal 4	5.11E-4	3E-6	6.22E-12	1.40E-4
Average				1.101E-4

have the lowest possible sensitivity because it must be able to detect very small changes in magnetic field. The average sensitivity from the four signals discussed in section 4.2.2 is $110 \mu\text{T}/\text{Hz}^{1/2}$. The sensitivity values for these signals are very poor compared to the device studied by Cochrane *et al.* [15], which had a sensitivity of $440 \text{ nT}/\text{Hz}^{1/2}$. Cochrane *et al.* even acknowledge that the sensitivity of their device must be improved in order to compare to other more expensive deep space magnetometers [15]. Therefore, the 4H-SiC pn junction studied in this lab would not be useful in a solid state magnetometer.

Comparing the NZFMR signals from the device in this paper to those from Cochrane *et al.* [15] revealed that the device in this paper gave much weaker signals. Cochrane *et al.* were able to get changes in recombination current ΔI of 300 pA with DC current on the order of 1 nA, which gives a SDR amplitude of $\Delta I/I = 0.37$. In this paper, the largest ΔI was 17.9 pA, with DC current on the order of 1 μA , which gives a SDR amplitude of $\Delta I/I = 5.96\text{E-}6$. This means that the NZFMR signals from the 4H-SiC BJT studied in this paper were very weak (6 orders of magnitude weaker), which helps explain why NHF interactions could not be detected. The signals were very small so the noise had a much larger effect and most likely drowned out the presence of hyperfine peaks. The weak signals of this lab are most likely not completely due to the device used. There are many variables in an EDMR spectrometer, as well as in the mounting of the device that affect the magnitude of the signal, and a researcher with more EDMR experience may have been able to get larger signals. However, three different spectrometers gave NZFMR signals with similar magnitudes, and multiple graduate students were consulted during the research process, so it is likely that the weak signals are partly due to the device being measured.

4.5 Low-Field SDR Measurements with Oscillating RF Field

The wide scan SDR signal with an oscillating RF field of frequency $\nu=151\text{MHz}$ is shown in Figure 32. There are wiggles in this response which at first glance could indicate a NHF pattern. However, upon further investigation on the derivative in Figure 33, there is little evidence of hyperfine peaks.

The wide scan reveals an interesting difference between the resonant response and the zero-field response which is that the resonant response increases the change in recombination current and the zero-field response decreases the change in recombination current. This effect is shown because in the two low-field responses, the signal increases, then decreases, whereas the zero-field response decreases first, then increases. Remember that the SDR signal is actually the derivative of the change in recombination current, so if you were to integrate the low-field response, the change in recombination current would be a positive peak, while the change in recombination current at zero-field would be a negative peak. This is an interesting response, and one that was not present in the only other paper that has looked at ZFSDR in SiC pn junctions by Cochrane and Lenahan [10]. In that paper, the zero-field response is the same orientation as the low-field resonant response.

Differences in the low-field resonant signals and the zero-field signals are expected because the respective mechanisms that cause the SDR response are different (these mechanisms

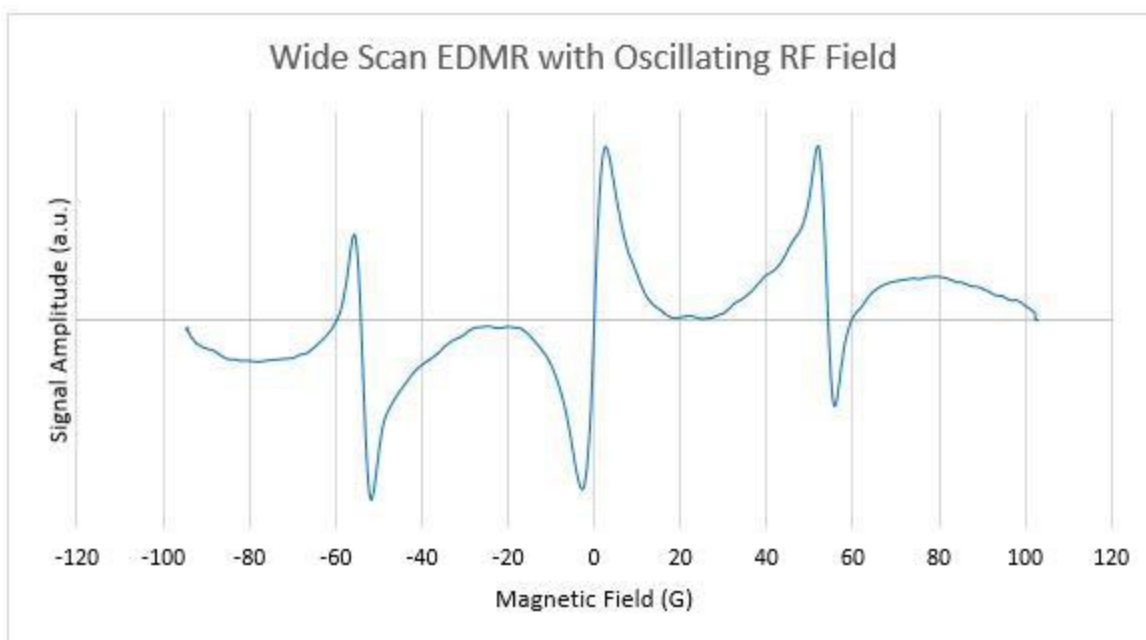


Figure 33: 200G wide SDR measurement with 151MHz RF oscillating field

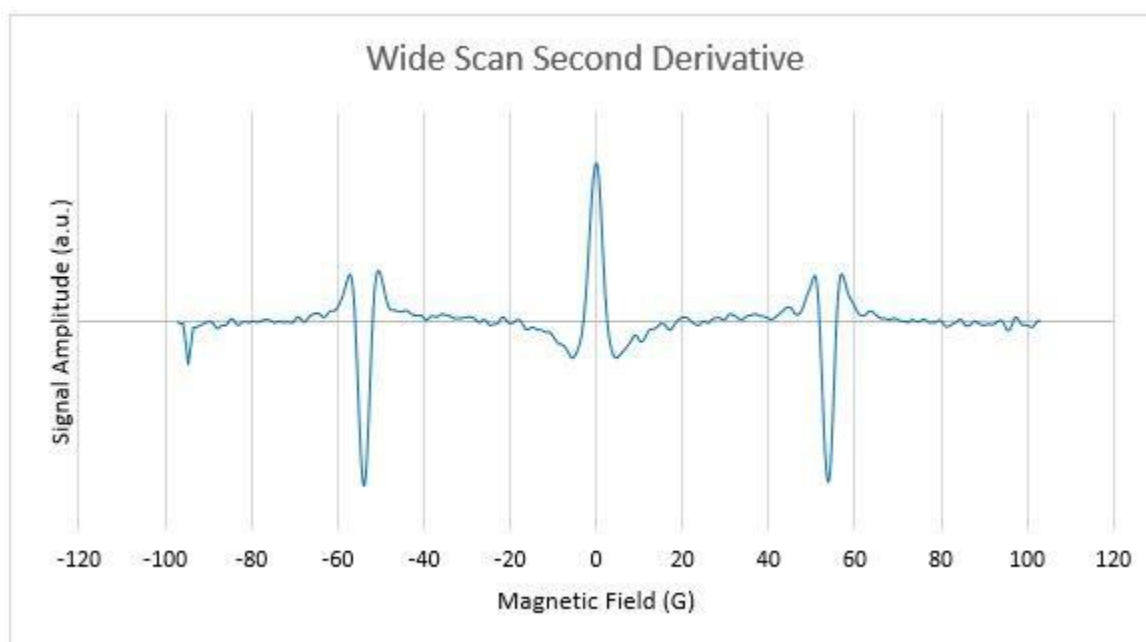


Figure 32: Derivative of SDR wide scan

are discussed in sections 2.5.2 and 2.5.3). The resonant response is due to electrons absorbing energy at resonance and flipping spins, which allows electrons and holes to recombine at recombination centers. The zero-field response is due to gradually modifying the orientation of the electron spin as zero-field approaches, which modifies the singlet-to-triplet ratio and

therefore changes the probability of recombination. The zero-field signal is thus wider than the low-field resonance signal in Figure 32 because the SDR mechanism is more gradual near zero-field. The different orientation of the signals (positive for resonance, negative for zero-field) could be an indication that the respective SDR responses are dominated by different defects in the depletion region. Because NZFMR measurements cannot extract a g -value, it is not possible to identify the dominate defect responsible for the signal, especially without a NHF pattern. However, the low-field SDR measurements do allow for the calculation of g -values, which can give some information about the dominate defect.

Three low-field SDR measurements were taken with the device oriented at three different angles. The low-field SDR measurement with the device at a 45 degree angle relative to the quasi-static magnetic field is shown in Figure 34. The SNR on this signal is fairly good, however, once again, no NHF interactions are apparent. In addition to the sharp central line response, there is also a broader response of the change in recombination current, which could be

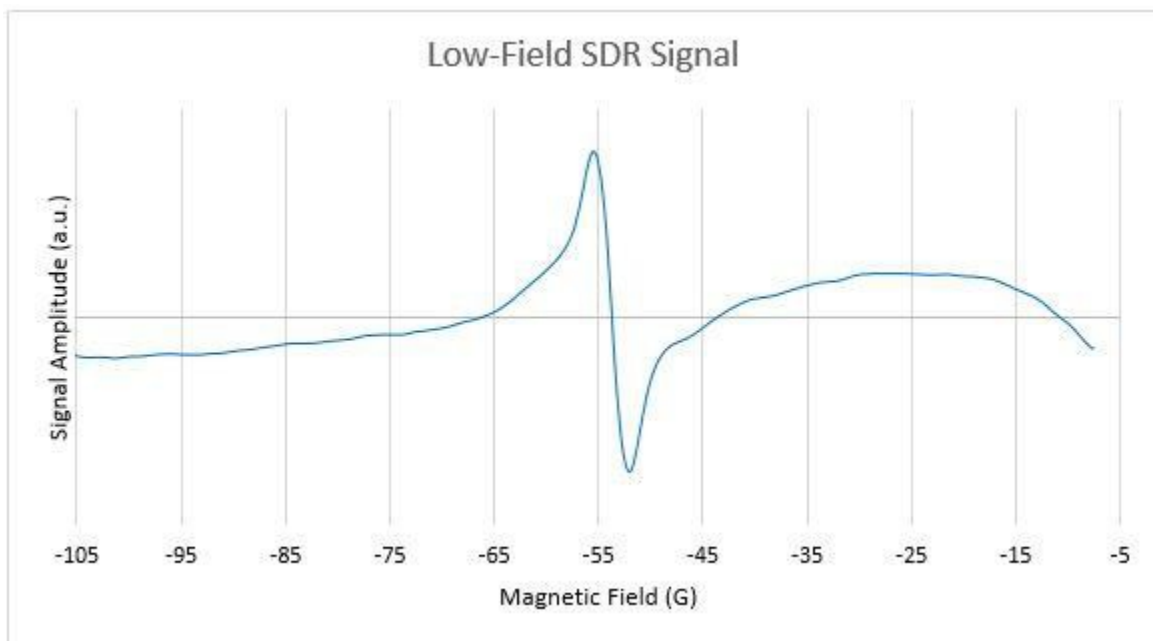


Figure 34: Low-Field SDR response with RF oscillating field of 151Hz

a real effect caused by the NZFMR phenomena. This broader response is more apparent in Figure 32. The g-values for the three low-field scans can be calculated using the equation discussed in section 2.5.2:

$$g = \frac{h\nu}{\beta H} \quad .$$

All the values on the right side are known: $h=6.626*10^{-34}$ J-s, $\beta = 9.274*10^{-28}$ J/G, $\nu = 151$ MHz, and H is the magnetic field at which resonance occurs. These g-values of low-field are different from g-values taken at high magnetic fields because the effects of low magnetic fields (<100G) are different than high magnetic field (>3000G). At high fields, the external field dominates the magnetic field experienced by the electron, while at lower fields, the local magnetic field effects of spin-orbit coupling have a larger effect on the spin orientation of the electron, and therefore the g values are different [16]. It would be extremely valuable to be able to pick up on NHF patterns at low-field because the magnitude of NHF splitting is equal at high and low magnetic fields. Therefore, the hyperfine patterns should be the same and high and low fields.

Unfortunately, no such hyperfine patterns were found in this research.

For the purposes of exercise, the g-values of the low-field EDMR measurements were still calculated. H was determined by finding the field value of the point of inflection of the SDR signal, or the field corresponding to the maximum of the derivative. The g-values of the three scans with the device at an angle of 0, 45, and 90 degrees are 2.00776, 2.00983, and 2.01625. It is reasonable to conclude that the dominate defect responsible for the SDR is anisotropic because the g-values are not the same for the three different angles. This is inconsistent with two papers discussed earlier the performed high-field EDMR on 4H-SiC BJT's and found isotropic g-values of 2.0026 and 2.0029 [11,12]. In fact, the g values are higher than any g values that could be found in literature for EPR and EDMR measurement on bulk 4H-SiC and 4H-SiC devices

(including pn junctions [10-12], and MOSFETs [16,17]). Almost all of g-values found in literature for 4H-SiC are between 2.002 and 2.004 [16-27]. Again, the low-field g values should be different from high-field g values, but the g values found in this experiment are much higher than any g values seen in literature, which indicates that these are not reliable for identifying defects. Anisotropic g values have been identified in some papers and are related to carbon vacancy defects [18,19,24,26]. The absence of any NHF patterns and the inconsistent g-values in the three low-field SDR traces make it not possible to identify the defect responsible for the SDR response.

4.6 Base-emitter Junction and Common Emitter Biasing

The SDR measurements on the base-collector junction were not able to resolve any NHF peaks. SDR measurements were also done on the base-emitter junction of the BJT, however these measurements were even more futile. As discussed in section 4.1 and shown in figure 20, the base-emitter junction had a much higher current than the base-collector junction. Very high DC currents are not ideal for SDR measurements because the high DC current creates lots of noise and overpowers the change in recombination current. NZFMR measurements were made on the base-emitter junction where the forward bias was varied from 2.0V to 2.6V in steps of 0.05V, but no signal was observed at any voltage. The currents in this range varied between 1mA and 3mA. The current that gave the best signals on the base-collector junction was around 3 μ A. The base-emitter was biased to produce this amount of DC current, which required a forward bias of only about 0.2V, but still no signal was present even after a long time of signal averaging.

Chapter 5

Conclusion and Future Work

Ultimately, the spectroscopic capabilities of low-field SDR and NZFMR were not properly demonstrated from these results, and no performance-limiting defects were identified in the 4H-SiC BJT. Although four NZFMR signals and three low-field SDR signals were measured, no NHF interactions were positively identified in any of them. The amplitude of the SDR response versus forward bias voltage did resemble the theoretical relationship between recombination current in the depletion region of a p-n junction which was promising because it proved that recombination centers in the depletion region were responsible for the response. However, without the presence of NHF patterns, the NZFMR response is not useful because it does not provide a g value. The g values were calculated for the low-field response, however these were not similar to any g values found in literature. When the NZFMR signals were analyzed in terms of the sensitivity of the solid-state magnetometer, it was determined that the 4H-SiC BJT being studied was giving very weak signals, and the NHF patterns were most likely lost in noise even after long periods of signal averaging. Unfortunately, by the time it was fully realized that the device being used would not give good data, there was little time to get different devices and repeat the experiment. There was also a limited number of spectrometers available for use in the laboratory because there are many undergraduates and graduate students who also have research to complete. Perhaps being able to signal average for many days at a time would have revealed NHF interactions, however it would not be courteous to other students who were waiting to use a spectrometer.

I plan to continue this work until graduation because I want to see the effort have meaningful results. Identifying NHF patterns in zero-field and low-field SDR measurements on a 4H-SiC BJT that can be compared to literature would be useful information to the scientific community and publishable research. There is only one paper published currently on this topic. I hope to obtain different 4H-SiC BJTs and repeat many of the experiments in this lab with the help of a graduate student who is working on a similar project. If this research is successful, it will be a meaningful contribution for identifying performance limiting defects in 4H-SiC BJTs, as well as for the development of low-field SDR and NZFMR as low cost and low energy alternatives to high-field EDMR.

Appendix

MATLAB Code For Plotting Theoretical Recombination Current

```

Na = 1e18; %Base doping
Nd = 5e15; %Collector Doping
ni = 5e-9; %intrinsic carrier concentration of 4H-SiC
k = 1.381e-23; %Boltzmann's Constant
T = 298; %Temperature
q = 1.6e-19;
Va= linspace(0,3.5,100);

V_bi = (k*T/q)*log(Na*Nd/ni^2); %built in voltage
Jr = sqrt(V_bi-Va).*exp(q.*Va/(2*k*T)); %Recombination current

plot(Va,Jr)
xlabel('Forward Bias (v)')
ylabel('Arbitrary Units')
title('Theoretical Recombination Current J_r versus Forward Bias V')

```

BIBLIOGRAPHY

1. Streetman, Ben G., and Sanjay Kumar Banerjee. *Solid State Electronic Devices*. 7th ed., Prentice-Hall, 2006.
2. A. S. Grove, *Physics and Technology of Semiconductor Devices* (Wiley, New York, 1967)
3. B. Van ZeghBroeck, "Chapter 4: p-n Junctions," *Principles of Semiconductor Devices*, 2011. [Online]. Available: https://ecee.colorado.edu/~bart/book/book/chapter4/ch4_2.htm
4. https://en.wikipedia.org/wiki/File:Bjt_equilibrium_bands_v2.svg
5. <https://coefs.uncc.edu/dlsharer/files/2012/04/C4.pdf>
6. Casady, J.B., and R. W. Johnson. "Status of silicon carbide (SiC) as a wide-bandgap semiconductor for high-temperature applications: A review." *Solid State Electronics*, vol. 39, No. 10, 1996, pp. 1409-1422., doi:10.1016/0038-1101(96)00045-7
7. Ostling, Mikael, et al. "SiC Power Devices — Present Status, Applications and Future Perspective." *2011 IEEE 23rd International Symposium on Power Semiconductor Devices and ICs*, 2011, doi:10.1109/ispsd.2011.5890778.
8. Zhang, Q. Jon, et al. "4H-SiC Bipolar Junction Transistors with a Current Gain of 108." *Materials Science Forum*, vol. 600-603, 2008, pp. 1159–1162., doi:10.4028/www.scientific.net/msf.600-603.1159.
9. P. M. Lenahan, A Brief Introduction to Electron Spin Resonance, 1st ed. Unpublished Manuscript, 2017
10. Cochrane, C. J., and P. M. Lenahan. "Zero-Field Detection of Spin Dependent Recombination with Direct Observation of Electron NHF Interactions in the Absence of

- an Oscillating Electromagnetic Field.” *Journal of Applied Physics*, vol. 112, no. 12, 2012, p. 123714., doi:10.1063/1.4770472.
11. Cochrane, C. J., et al. “Deep Level Defects Which Limit Current Gain in 4H SiC Bipolar Junction Transistors.” *Applied Physics Letters*, vol. 90, no. 12, 2007, p. 123501., doi:10.1063/1.2714285.
 12. Cochrane, Corey J., et al. “Direct Observation of Lifetime Killing Defects in 4H SiC Epitaxial Layers via Spin Dependent Recombination in Transistors.” *Materials Science Forum*, vol. 615-617, 2009, pp. 299–302., doi:10.4028/www.scientific.net/msf.615-617.299.
 13. Swartz, Harold M., et al. *Biological Applications of Electron Spin Resonance*. Wiley, 1972.
 14. N. J. Harmon, M. E. Flatté, "Spin-flip induced magnetoresistance in positionally disordered organic solids", *Phys. Rev. Lett.*, vol. 108, no. 18, pp. 186602-1-186602-5, May 2012.
 15. Cochrane, C. J. et al. “Vectorized magnetometer for space applications using electrical readout of atomic scale defects in silicon carbide.” *Sci. Rep.* 6, 37077; doi: 10.1038/srep37077 (2016).
 16. C. J. Cochrane, P. M. Lenahan, and A. J. Lelis “The effect of nitric oxide anneals on silicon vacancies at and very near the interface of 4H SiC metal oxide semiconducting field effect transistors using electrically detected magnetic resonance” *Appl. Phys. Lett.* 102, 193507 (2013); <https://doi.org/10.1063/1.4805355>
 17. Anders, Mark A., et al. “Relationship Between the 4H-SiC/SiO₂ Interface Structure and Electronic Properties Explored by Electrically Detected Magnetic Resonance.” *IEEE*

Transactions on Electron Devices, vol. 62, no. 2, 2015, pp. 301–308.,

doi:10.1109/ted.2014.2364722.

18. Aichinger, T., et al. “A nitrogen-related deep level defect in ion implanted 4H-SiC pn junctions—A spin dependent recombination study” *Appl. Phys. Lett.* 100, 112113 (2012); <https://doi.org/10.1063/1.3695330>
19. Umeda, T., et al. “EPR and Theoretical Studies of Negatively Charged Carbon Vacancy in 4H-SiC.” *Physical Review B*, vol. 71, no. 19, 2005, doi:10.1103/physrevb.71.193202.
20. Mizuochi, N., et al. “EPR Studies of the Isolated Negatively Charged Silicon Vacancies in 4H- and 6H-SiC: Identification of C_{3v} symmetry and Silicon Sites.” *Physical Review B*, vol. 68, no. 16, 2003, doi:10.1103/physrevb.68.165206.
21. Mizuochi, N., et al. “Continuous-Wave and Pulsed EPR Study of the Negatively Charged Silicon Vacancy with $S=3/2$ and C_{3v} Symmetry in n-type 4H-SiC.” *Physical Review B*, vol. 66, no. 23, 2002, doi:10.1103/physrevb.66.235202.
22. Janzén, Erik, et al. “The Silicon Vacancy in SiC.” *Materials Science Forum*, vol. 615-617, 2009, pp. 347–352., doi:10.4028/www.scientific.net/msf.615-617.347.
23. Sörman, E., et al. “Silicon Vacancy Related Defect in 4H and 6H SiC.” *Physical Review B*, vol. 61, no. 4, 2000, pp. 2613–2620., doi:10.1103/physrevb.61.2613.
24. Orlinski, S. B., et al. “Silicon and Carbon Vacancies in Neutron-Irradiated SiC: A High-Field Electron Paramagnetic Resonance Study.” *Physical Review B*, vol. 67, no. 12, 2003, doi:10.1103/physrevb.67.125207.
25. Son, N. T., et al. “Silicon Antisite in 4H-SiC.” *Physical Review Letters*, vol. 87, no. 4, 2001, doi:10.1103/physrevlett.87.045502.

26. Son, N. T., et al. "Carbon Vacancy-Related Defect in 4H and 6HSiC." *Physical Review B*, vol. 63, no. 20, 2001, doi:10.1103/physrevb.63.201201.
27. Son, N. T., et al. "Divacancy in 4H-SiC." *Physical Review Letters*, vol. 96, no. 5, 2006, doi:10.1103/physrevlett.96.055501.

ACADEMIC VITA

Education

Bachelor of Science in Engineering Science

Graduation May 2019

The Pennsylvania State University, University Park, PA
Schreyer Honors College

Engineering Experience

DC Test Engineer Intern at Qorvo, Richardson, TX

May-August 2018

- Wrote a new DC test algorithm in C that reduced test time by 65%
- Analyzed DC Probe data using Tibco Spotfire in order to diagnose test issues
- Created specification sheets and test software programs for new GaAs/GaN devices

Undergraduate Researcher at Semiconductor Spectroscopy Lab

January 2018-Present

- Operate electronically detected magnetic resonance spectrometers in order to understand the structure and defects of semiconductor devices
- Senior Thesis Topic: Investigating Performance Limiting Defects in SiC BJTs using EDMR

Engineering Intern at C&K Plastics, Metuchen, NJ

June-August 2017

- Created CNC programs from a computer model using Mastercam CAD software
- Operated CNC milling machines to cut CNC fixtures and patterns for new parts

ENGR 118- Impact of Chinese Culture on Engineering

May-June 2017

- Learned about Chinese history and culture and how it affects business and engineering by visiting schools, companies, structures and historical sites in 9 Chinese cities

Work Experience

CNC Setup at C&K Plastics, Metuchen, NJ

May-August 2016

Molder at C&K Plastics, Metuchen, NJ

Summer 2014, 2015

Activities

Tau Beta Pi, Public Relations Chair

January 2018-Present

- Send out a weekly newsletter to inform members and candidates of upcoming events
- Design posters and videos to advertise the club on campus